

1-1-2008

Titanium hydride up to 90 GPA: Synchrotron X-ray diffraction studies

Patricia E Kalita
University of Nevada, Las Vegas

Follow this and additional works at: <https://digitalscholarship.unlv.edu/rtds>

Repository Citation

Kalita, Patricia E, "Titanium hydride up to 90 GPA: Synchrotron X-ray diffraction studies" (2008). *UNLV Retrospective Theses & Dissertations*. 2295.
<http://dx.doi.org/10.25669/5he1-t9bq>

This Thesis is protected by copyright and/or related rights. It has been brought to you by Digital Scholarship@UNLV with permission from the rights-holder(s). You are free to use this Thesis in any way that is permitted by the copyright and related rights legislation that applies to your use. For other uses you need to obtain permission from the rights-holder(s) directly, unless additional rights are indicated by a Creative Commons license in the record and/or on the work itself.

This Thesis has been accepted for inclusion in UNLV Retrospective Theses & Dissertations by an authorized administrator of Digital Scholarship@UNLV. For more information, please contact digitalscholarship@unlv.edu.

TITANIUM HYDRIDE UP TO 90 GPA: SYNCHROTRON

X-RAY DIFFRACTION STUDIES

by

Patricia E. Kalita

Bachelor of Sciences,
University of Nevada Las Vegas
2005

Baccalauréat Scientifique,
Lycée Louis le Grand, Paris, France
1999

A thesis submitted in partial fulfillment
of the requirements for the

Master of Sciences Degree in Physics
Department of Physics and Astronomy
College of Sciences

Graduate College
University of Nevada, Las Vegas
May 2008

UMI Number: 1456344

INFORMATION TO USERS

The quality of this reproduction is dependent upon the quality of the copy submitted. Broken or indistinct print, colored or poor quality illustrations and photographs, print bleed-through, substandard margins, and improper alignment can adversely affect reproduction.

In the unlikely event that the author did not send a complete manuscript and there are missing pages, these will be noted. Also, if unauthorized copyright material had to be removed, a note will indicate the deletion.

UMI[®]

UMI Microform 1456344

Copyright 2008 by ProQuest LLC.

All rights reserved. This microform edition is protected against unauthorized copying under Title 17, United States Code.

ProQuest LLC
789 E. Eisenhower Parkway
PO Box 1346
Ann Arbor, MI 48106-1346

Copyright by Patricia E. Kalita 2008
All Rights Reserved



Thesis Approval

The Graduate College

University of Nevada, Las Vegas

February 25, 2008

The Thesis prepared by

Patricia E. Kalita

Entitled

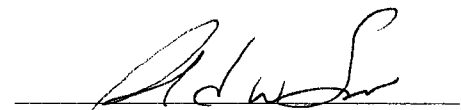
Titanium Hydride up to 90 GPa: Synchrotron X-Ray Diffraction Studies

is approved in partial fulfillment of the requirements for the degree of

Master of Sciences in Physics



Examination Committee Chair



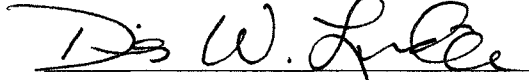
Dean of the Graduate College



Examination Committee Member



Examination Committee Member



Graduate College Faculty Representative

ABSTRACT

Titanium Hydride up to 90 GPa: Synchrotron X-Ray Diffraction Studies

by

Patricia E. Kalita

Dr. Andrew L. Cornelius, Examination Committee Chair
Associate Professor of Physics
University of Nevada, Las Vegas

The structure and behavior of titanium hydride was studied on compression to about a megabar. Angle-dispersive as well as energy-dispersive synchrotron X-ray diffraction studies were carried out in situ, in diamond anvil cells, in several compression and decompression sequences. A phase transition from a cubic to a tetragonal structure was observed. The pressure evolution of the diffraction patterns revealed that the cubic (Fm-3m) to tetragonal (I4/mmm) phase transition occurs at about 0.6 GPa. The transition was found to be reversible on decompression from 34 GPa but irreversible on decompression from 90 GPa. The influence of the pressure transmitting medium on the pressure-induced structural transformations of TiH₂ was also examined. An equation of state fit of the evolution of unit cell volume as a function of pressure, up to 90 GPa yielded a zero pressure bulk modulus $K_0=143(7)$ GPa, and its pressure derivative $K'_0=3.0(0.1)$ for the high-pressure tetragonal phase of TiH₂.

TABLE OF CONTENTS

ABSTRACT.....	iii
LIST OF FIGURES.....	vi
ACKNOWLEDGEMENTS.....	vii
CHAPTER 1 INTRODUCTION.....	1
CHAPTER 2 LITERATURE OVERVIEW.....	5
2.1. Hydrides	5
2.1.1. Definition	5
2.1.2. Classification	6
2.1.3. Diffusion	7
2.1.4. Properties of Hydrides	7
2.1.5. Production.....	8
2.1.6. Applications of Hydrides	9
2.2. Hydrogen Storage: an Application with Strategic Potential	11
2.3. Titanium Hydride.....	13
2.3.1 Interaction of Ti with H ₂ and Properties of TiH ₂	13
2.3.2 Catalytic Action of TiH ₂	16
2.4. The Structure of Crystals	17
2.5. Overview of X-Ray Diffraction	19
2.5.1 Production of X-rays	20
2.5.2. The Bragg Equation	21
2.5.3. The Laue Method	23
2.5.4. The Debye-Scherrer Method	23
2.6. Theory of X-Ray Diffraction	24
2.6.1. The Reciprocal Space	25
2.6.2. The Laue condition.....	27
2.6.3. The Bragg Equation	30
2.6.4. Atomic scattering factor	30
2.6.5. Structure Factor	32
2.6.6. Temperature Factor	34
2.7. High-Pressure in Materials Science	36
2.7.1. Introduction	36
2.7.2. The Progress and Diversification of High-Pressure Research	37
2.7.3. The Effect of Pressure on Matter.....	38

2.7.4.	At the Heart of High-Pressure Research: the Diamond Anvil Cell	40
2.7.5.	How is Pressure Measured in a Diamond Anvil Cell	41
2.8.	Synchrotron X-Ray Diffraction.....	43
2.8.1.	A Brief History of Synchrotrons	43
2.8.2.	Productions of Synchrotron X-rays: Bending Magnets, Undulators.....	44
2.8.3.	The Advanced Photon Source at Argonne National Laboratory	45
CHAPTER 3	EXPERIMENTAL	49
3.1.	Ambient Pressure X-ray Diffraction	49
3.2.	High-Pressure Synchrotron X-Ray Diffraction	49
3.2.1.	Energy-Dispersive X-Ray Diffraction (EDXRD).....	50
3.2.2.	Angle-Dispersive X-Ray Diffraction (ADXRD)	51
CHAPTER 4	RESULTS	55
4.1.	On the structure of TiH_2	55
4.2.	Ambient Pressure, High-Temperature X-ray Diffraction	57
4.3.	Energy-Dispersive Synchrotron X-Ray Diffraction of TiH_2 to 34 GPa	61
4.4.	Angle-Dispersive Synchrotron X-Ray Diffraction of TiH_2 to 90 GPa	64
CHAPTER 5	DISCUSSION AND CONCLUSIONS	70
5.1.	Equation of State of Titanium Hydride	70
5.1.1.	Equations of State for Solids at Extremely High-pressures	70
5.1.2.	Birch-Murnaghan Equation of State of TiH_2 with EDXRD	77
5.1.3.	Birch-Murnaghan Equation of State of TiH_2 with ADXRD.....	81
5.1.4.	Bulk Modulus of TiH_2 : a Comparison of EDXRD and ADXRD Data	87
5.2.	Phase Transitions	90
5.2.1.	Types of Phase Transitions.....	90
5.2.2.	Titanium Hydride	91
5.2.3.	Phase Diagram of TiH_2	93
5.3.	ADXRD versus EDXRD	93
5.4.	Issues: Texture, Pressure-Transmitting Media and Pressure.....	95
5.4.1.	Preferred Orientation	95
5.4.2.	On Successfully Achieving Extreme Pressures.....	97
5.4.3.	The Quest for Hydrostatic Conditions and Measuring Pressures.....	98
5.5.	Conclusions.....	101
REFERENCES	104
VITAE	109

LIST OF FIGURES

Figure 1	Schematic of sorption of H ₂ into a metal lattice	14
Figure 2	Bragg's law for x-ray diffraction	22
Figure 3	Schematic of a reciprocal lattice	28
Figure 4	Schematic of crystal lattice plains	29
Figure 5	Decomposition of the position vector in a unit cell	31
Figure 6	The principle behind a Diamond Anvil Cell	40
Figure 7	The Advanced Photon Source	46
Figure 8	Set up of station ID-B at Sector	52
Figure 9	Diamond anvil cell	53
Figure 10	Models of Titanium Hydride	55
Figure 11	Conventional XRD measurements versus temperature	58
Figure 12	Rietveld refinement at 25°C.....	59
Figure 13	Rietveld refinement at 17°C.....	60
Figure 14	EDXRD measurements up to 34 GPa.....	63
Figure 15	Rietveld refinement of an ambient pressure ADXRD pattern	65
Figure 16	ADXRD measurement up to 21 GPa	66
Figure 17	ADXRD measurement up to 90 GPa	67
Figure 18	Rietveld refinement of a 2.2 GPa pattern.....	77
Figure 19	Rietveld refinement of a 34 GPa pattern.....	78
Figure 20	Unit cell parameters from EDXRD measurements.....	79
Figure 21	Unit cell volume from EDXRD measurements	80
Figure 22	Rietveld refinement of a 0.6 GPa pattern from ADXRD measurements	82
Figure 23	Rietveld refinement of a 90 GPa pattern from ADXRD measurements	83
Figure 24	Unit cell parameters from ADXRD measurements	84
Figure 25	Unit cell volume from ADXRD measurements	86
Figure 26	Model of the non-isomorphic subgroup relation	92
Figure 27	Partial phase diagram of titanium hydride	93
Figure 28	Selected ADXRD patterns collected with the image plate detector	96

ACKNOWLEDGEMENTS

Work at UNLV was supported by DOE award No. DEFG36-05GO08502. The UNLV High Pressure Science and Engineering Center was supported by the US Department of Energy, National Nuclear Security Administration, under Cooperative Agreement DE-FC08-01NV14049. Portions of this work were performed at HPCAT (Sector 16), Advanced Photon Source (APS), Argonne National Laboratory. Use of the HPCAT facility was supported by DOE-BES, DOE-NNSA (CDAC), NSF, DOD –TACOM, and the W.M. Keck Foundation. Use of the APS was supported by DOE-BES, under Contract No. W-31-109-ENG-38.

This work is dedicated to my best friend, Kristina L-K. Special thanks to my advisor, Prof. A. Cornelius and my committee members, Prof. M. Nicol, Prof. L. Zane, and Prof. D. Lindle. I also wish to thank all my family and my friends from UNLV and other parts of the world, who kept my spirits up during this process as well as to the invaluable Dr. S. Sinogeikin (APS-HPCAT).

CHAPTER 1

INTRODUCTION

Hydrogen can be used as source of clean, renewable energy in practical applications under rather stringent pressure and temperature operating conditions. One of the key, and most challenging aspects for a practically achievable and successful transition to an economy based on hydrogen is on-board hydrogen storage.¹

Metal hydrides have been the subject of scientific investigations for several years.^{2,3} The currently emerging picture places complex metal hydrides as the leads in the race for high volumetric density storage materials. Simple binary hydrides, on the other hand, may play an assisting role in the storage of hydrogen. According to the US Department of Energy, basic research into the physical, chemical and mechanical properties of metal hydrides is indispensable for enabling potential breakthroughs needed to make the hydrogen economy a reality.¹

The U. S. Department of Energy states that by “promoting broad interdisciplinary efforts, strong coordination between the basic and applied sciences, (...) scientific breakthroughs in one area can be leveraged to advance progress in others”.¹ The statement continues further and points out that “(b)asic research is essential for identifying novel materials and processes that can provide potential breakthroughs needed to meet the Hydrogen Fuel Initiative goals.” Also “(a) basic understanding of the

physical, chemical, and mechanical properties of metal hydrides and chemical hydrides is needed.” In fact there exists a real need of basic and interdisciplinary research in order to promote the evolution of knowledge needed to make hydrogen storage technically and commercially viable for vehicular applications.

In the past several years it has become possible to achieve, in the laboratory, extremely high-pressures (superior to what can be achieved with the temperature parameter). The multimegabar pressures now achievable correspond to a volume compression in excess of an order of magnitude, which can reveal a wealth of information about molecular materials.⁴ The pressure-volume work (free energy change) can be of up to 10 eV which exceeds the strongest molecular bonds. Among the effects of such extreme compression there are: changes in bonding patterns, phase transitions, chemical reactions, quantum effects, changes in chemical properties, changes in physical properties. Pressure also modifies chemical affinities and hence reactivities, and in this way new materials with unusual combination of physical and chemical properties can be formed. High-pressure x-ray diffraction studies of materials (bulk- and nano-structures) are critical to identifying new equilibrium and metastable states that can be accessed, as these materials are compressed to very small volumes.^{4,5}

The metal hydride selected for the presented high-pressure synchrotron radiation-based structural studies is titanium hydride (TiH_2). This is a simple binary hydride interesting not as a storage material, but as a catalyst enhancing storage properties of other hydrides and other materials. In fact, it was recently found that Ti hydrides can act as active species to catalyze the reversible dehydrogenation of carbon

nanotubes as well as other hydrides.⁶⁻⁸ The basic science interest of this project lies in investigating the structure and especially the high-pressure behavior of TiH_2 in order to identify phase transitions and possibly new quenchable phases.

It should be pointed out that there is no certainty as to whether metal hydrides, either simple or complex, will actually achieve the high volumetric and gravimetric densities required for mobile applications. What is certain, however, is that at the current state of knowledge, fundamental research in multiple directions is still of primordial importance and it is in this spirit that the presented *Master of Sciences* research was envisioned and carried out.

The presented *Master of Sciences Thesis* is structured in five chapters as follows.

Chapter 2 introduces all the conceptual elements involved in the present research. Since the material investigated is TiH_2 , an overview of hydrides is presented, including fabrication, properties and applications. The issues and the advances in metal hydrides studies for hydrogen storage are also laid out. Subsequently the technique of X-ray diffraction is presented including the production of X-rays as well as elements of crystallography. The object of this work is the study of TiH_2 to extreme pressures (up to 90 GPa). Thus Chapter 2 also outlines the effects of high-pressures on materials, with specifics on how high-pressures are achieved in the laboratory and how materials under high-pressures are investigated. Finally, since X-ray diffraction studies at high-pressures require very bright and highly focused radiation, synchrotron radiation is introduced at the end of Chapter 2 with production of X-rays as well as the synchrotron storage ring where the present studies were carried out.

Chapter 3 presents the multi-technique approach used for these structural studies. First, the temperature-variable conventional X-ray diffraction studies are described. Next, the details of the high-pressure synchrotron radiation-based X-ray diffraction experiments are introduced. Here the two experimental techniques used are described: energy-dispersive X-ray diffraction (EDXRD) as well as high-resolution angle-dispersive X-ray diffraction (ADXRD).

Chapter 4 outlines the results of the multi-technique investigations. First, results of the conventional x-ray diffraction at moderately high temperatures are outlined. Next, the initial high-pressure, energy-dispersive synchrotron X-ray diffraction studies up to 34 GPa are presented. The outline of key results continues with two series of high-resolution angle-dispersive X-ray diffraction studies of TiH_2 on compression/decompression up to 21 GPa and up to 90 GPa.

Chapter 5 contains a discussion of the results. First the observed phase transitions and structural refinements are presented. Next the mechanical properties of TiH_2 are analyzed using specific mathematical formalism. A comparison of the two experimental techniques – EXRD and ADXRD – is presented in the light of obtained results. Issues and limitations of the experimental techniques, such as hydrostaticity and texture, are discussed. Remarks are offered on the experimental challenges of attaining pressures in the megabar region. Finally the key conclusions of this *Master of Sciences Thesis* research are presented.

CHAPTER 2

LITERATURE OVERVIEW

2.1. Hydrides

2.1.1. Definition

A metal hydride consists of a metal lattice with dissolved hydrogen atoms located at interstitial sites. The dissolution of hydrogen in a metal lattice and the subsequent formation of a metal hydride perturbs considerably the electrons and phonons of the host metal. The amount of hydrogen absorbed in metals is proportional to the square root of the external pressure of hydrogen gas.⁹ This indicates that the absorbed hydrogen is dissociated into atoms. All metals have been classified into good or poor absorbers of hydrogen. Metals such as Pd or Ti are good absorbers since they can absorb large quantities of hydrogen at relatively low temperatures and pressures. With increasing temperature the concentration of hydrogen will in fact decrease.⁹ The concentration of saturation absorption of hydrogen in good absorbers goes as high as 100 at. % or 200 at. % of metallic atoms and the resulting hydrides are represented by formulas such as PdH or TiH₂.⁹ Metals that are poor absorbers, on the other hand, absorb small amounts of hydrogen and need higher temperatures to increase absorption.⁹

2.1.2. Classification

Hydrides are classified according to the nature of their hydrogen bond into 3 categories: covalent (volatile), saline (ionic) and metallic.¹⁰⁻¹² Covalent or volatile hydrides can be solid, liquid or gaseous. The bond between the element and hydrogen is of the non-polar electron-sharing type, where the valence electrons are shared on a fairly equal basis. The absence of strong intermolecular forces results in the high degree of volatility and low melting point of covalent hydrides. Saline hydrides are compounds formed by the reaction of strongly electropositive alkali metals and alkaline-earth metals with hydrogen, which becomes strongly electronegative because of the transfer of electrons. Saline hydrides are highly polar, because the bond results from strong electrostatic forces of the dissimilar electric charges of the two ions.

Metallic hydrides are formed by the transition metals of the periodic table, and possess metallic properties such as high thermal conductivity and electrical resistivity. Because of the wide homogeneity ranges of most metallic hydrides they have been sometimes considered to be solid solutions of hydrogen in the metal. However such classification is not correct. In fact crystal structures of the hydrides are different from those of the parent metal. In the case of TiH_2 for example, titanium and hydrogen atoms occupy distinct crystallographic sites in the lattice (Wyckoff positions 4a and 8c, respectively) and titanium hydride (*fcc*) forms a distinct compound form titanium metal (*hcp*).

Bonding in metal hydrides can occur following one of three models, which classify the hydrogen in the hydride: (1) protonic hydrogen, where the electron of H is

used to fill the d-band of the metal – this model assumes that the hydride is an alloy of hydrogen with metal; (2) covalently bound hydrogen; (3) anionic hydrogen – a mixture of ionic bonds (where electrons from the metal are transferred to the hydrogen) and metallic bonds.¹⁰⁻¹² This classification however, is somewhat arbitrary since no compound contains purely one type of bond. In metallic hydrides such as TiH_2 the d-band is less than half-filled so following Hund's rule electrons from H atoms are added to the d-band of the metal so the hydrogen is protonic in this metal hydride.¹⁰

2.1.3. Diffusion

Diffusion of hydrogen in hydrides takes place by the movement of lattice defects. The hydrogen atom can either jump from a normal tetrahedral site to an adjoining empty tetrahedral site in the (100) direction, or it can jump in the (111) direction through an octahedral position into a vacant tetrahedral site.¹⁰ Octahedral interstitial sites are vacant because of the effect of H-H blocking, where one H atom in an interstitial site will block all near interstitial sites from filling with hydrogen within the limits of a blocking radius ($\sim 2.135 \text{ \AA}$). This radius is much greater than the shortest tetrahedral-to-octahedral interstitial site distance, which results in only the tetrahedral interstitial sites being occupied.¹³

2.1.4. Properties of Hydrides

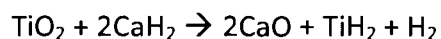
Two measures of capacity of a hydride are used.² One is the atomic H/M ratio or weight percent, which includes both H and M in the denominator of the calculation. Hydrogen content can also be expressed as the number of H atoms per unit volume (ex. cm^3) labeled as $\Delta N_{\text{H}}/V$, where ΔN represents the reversible capacity. This measure

represents the volumetric density in crystal terms and hence does not include the void which is important from the point of view of a container. Activation is the procedure needed to hydride a metal the first time and bring it up to maximum H-capacity and hydriding / dehydriding kinetics. The ease of initial H₂ penetration depends on surface structures and barriers, such as dissociation catalytic species and oxide films. A second stage of activation involves internal cracking of metal particles to increase reaction surface area. Decrepitation means the self-pulverization of large metal particles into powder, a common phenomenon that results from a combination of hydriding volume change and the brittle nature of hydriding alloys (especially when they contain some H in solution). Cyclic stability is important and widely variable from alloy to alloy. Alloys and intermetallic compounds are usually metastable relative to disproportionation, the tendency to break up metallurgically to form stable, not easily reversed hydrides. Even if very pure H is used, disproportionation can occur with a resultant loss of reversible capacity. Safety of a hydride encompasses toxicity as well as pyrophoricity, or the tendency for a hydride powder to burn when suddenly exposed to air.

2.1.5. Production

Several preparation methods of metallic hydrides exist. In the direct combination of elements, diffusion of hydrogen occurs at the surface of a previous cleaned metal. Uptake of hydrogen can be improved by heating below the dissociation temperature and by increasing the pressure of H₂ gas. The mechanism of hydriding of a parent metal follows four steps.¹⁰ First, hydrogen is adsorbed on the surface and it is dissociated into adsorbed hydrogen atoms. Next, the hydrogen atoms diffuse into the bulk of the metal.

This is the step where the system metal+hydrogen can be called a 'solid solution'. Finally, the hydrogen-saturated metal reacts with additional adsorbed hydrogen to form a hydride layer. As more hydrogen diffuses through the newly formed hydride layer it reacts with the parent metal thus spreading the metal hydride formation. The newly formed hydride can either adhere to the metal or flake off, thus speeding the reaction of formation (which is then a surface process).¹⁰ Some metallic hydrides can also be prepared following the reduction of oxides with another hydride:



Titanium hydride can be fabricated in several ways. One of the simplest methods consists in heating to over 200°C and subsequently cooling titanium metal in a hydrogen atmosphere.^{10, 11} Like for other transition metals, the initial diffusion of hydrogen into the metal is slow until the metal structure has been opened up by the process of lattice expansion. Rifts and structure defects allow hydrogen to penetrate the metal through first a rapid diffusion followed by slow penetration as the metal alloys with hydrogen.^{10, 11} Titanium will lose most of its hydrogen at about 400°C and will be completely outgassed 800-1000°C.

2.1.6. Applications of Hydrides

Titanium hydride can be used as a source of pure titanium metal. It can be employed as a coating of corrosion resistant titanium on the surface of another metal.^{10, 11} Titanium hydride can be added to powder mixtures used in the fabrication of articles by the powder metallurgy technique where its role is to increase the density of the compacted powder. It can also prevent the oxidation of the metal powder during the

sintering process.^{10, 11} In the process of fabrication of electronic tubes, titanium hydride is deposited on a ceramic surface and then used as a base for soldering metal parts to the ceramic.^{10, 11}

One of the applications of hydrides consists in using thermal swings of hydride beds in the compression of gaseous H. Hydrides are employed in the separation of either H₂ from other gasses or in the separation of H-isotopes. Less common applications comprise cryocooling, chemical catalysis (see section 2.3.1. below), synthesis of ammonia and methane and diamond synthesis.²

There are several further applications comprised under the name of 'closed thermodynamic systems' where H₂ is a "working fluid" which is contained in closed systems. These applications include: heat engines, where heat is converted to mechanical energy in an expansion engine (this category includes temperature sensors); storage of heat (ex. solar); heat pumps, where low-temperature heat is 'upgraded' to higher temperature; refrigerators, where heat is converted to refrigeration.²

Metal hydrides can also be applied in the development of cheap, small, and reliable hydrogen detectors. They have to enable hydrogen detection well before the 4% explosion limit if hydrogen is to become a socially acceptable energy source in the future. Current hydrogen detection systems are too large and too expensive, not safe and those that are small have too long detection times.¹⁴ Metal hydrides can be used as switchable mirrors with a very high optical contrast.¹⁴ In fact it was recently shown that a fiber optic hydrogen detector with a high optical contrast can be made using an Mg-Ti active material.¹⁴ The optical reflectance of the Mg-Ti film decreases by an order of

magnitude when hydrogen is applied (from 60% to 7%). Moreover this hydrogenated state is strongly absorbing over a wide spectral range. The change in reflectance is due to the intrinsic light absorption in the hydride. This is convenient for the design of hydrogen sensors, but also other applications such as solar absorbers or smart windows are being considered for the Mg–Ti active material.¹⁴

2.2. Hydrogen Storage: an Application with Strategic Potential

Hydrogen would be ideal as a synthetic fuel because it is lightweight, highly abundant and its only byproduct in the reaction of oxidation is water.³ The most common method to store hydrogen in gaseous form is in steel tanks, although lightweight composite tanks designed to endure higher pressures are becoming more and more common. Cryogas, gaseous hydrogen cooled to near cryogenic temperatures, is another alternative that can be used to increase the volumetric energy density of gaseous hydrogen.^{1,3}

Another form of hydrogen storage is as solid hydride. Most of the 91 natural elements above H will hydride under appropriate conditions. Unfortunately, the pressure-composition-temperature (PCT) properties are not very convenient relative to the 1–10 atm, 0–100°C range of utility required for practical applications.² Using hydrides as “vessels” for storing hydrogen in a manner that does not require an expensive and dangerous tank is a relatively new (prospective) application for hydrides. If the application is in one site (a factory for example) then large amounts are not an issue but what is important is the cost of the hydride. Vehicular applications, on the

other hand, require high weight percent (or gravimetric density) of stored hydrogen in order to minimize the on board weight and the associated energy consumption. Ideally any application of a hydrogen storage material requires high storage capacity but at low system weight. This in turn entails strong chemical bonding and light and stable storage materials. On the other hand fast sorption/desorption of hydrogen and cycling capability, which are also necessary for realistic practical applications, require weak chemical bonding, fast kinetics, and less diffusion resistance, as might be found in surface adsorption. This constitutes a tradeoff between high capacity and fast kinetics.

¹⁵ Other sought-after properties of hydrides for either mobile or static hydrogen storage applications are: easy activation to minimize container pressure and temperature requirements; in the case impurities such as air are introduced, a good resistance to gaseous impurities is desirable; PCT properties should be roughly in the ambient temperature and pressure area so that waste heat from the environment or vehicle engine (or fuel cell) can be used for endothermic H desorption. ² In summary, materials capable of storing hydrogen with high gravimetric and volumetric density, operating under ambient thermodynamic conditions, and exhibiting fast hydrogen sorption kinetics are essential for practical applications. ³

Hydrogen can be stored in solid materials either in atomic or molecular form. Storage of hydrogen in molecular form has an advantage in that molecular hydrogen has fast kinetics. However, its bonding is very weak and desorption can take place at low temperatures. Various simple and complex hydrides ^{2, 3, 12, 16-20} have been the focus of extensive investigations with the goal of finding one that will have high gravimetric

density and will operated in the narrow P and T window required by practical applications.

The U.S. Department of Energy (DOE) has established a multistage target for hydrogen storage capacity for fuel-cell applications for an on-board hydrogen storage system: 4.5 wt % by 2007, 6 wt % by 2010, and 9 wt % by 2015, at moderate temperatures and pressures (0-100° C and 1-10 atm.).¹

With a nominal 7.6 wt % of hydrogen MgH_2 as well as magnesium-based alloys are some of the most promising hydrides for hydrogen storage.^{15, 17, 18, 21-23} In spite of their low cost, however magnesium-based alloys suffer from sluggish sorption kinetics and so their hydrogenation and dehydrogenation require significant activation energy (in the form of high temperatures).¹⁵ The same issue was observed for many other hydrides and showed the need for catalysts. In search for alternate hydrogen storage candidates, considerable attention has also been focused on porous materials such as clathrates, zeolites, carbon nanotubes, fullerenes and nanocomposites.^{24, 25}

2.3. Titanium Hydride

2.3.1. Interaction of Ti with H_2 and Properties of TiH_2

Like many of the metallic hydrides, TiH_2 has a dull metallic appearance. In stoichiometric composition of titanium hydride the valance of Ti is less than the usual oxidation state (+4). TiH_2 is fairly stable in air at room temperature and will only react at elevated temperatures.¹⁰ Like other metal hydrides TiH_2 displays some properties which are very different with respect to the parent metal. Among some general trends are the

modification of the crystal structure from hcp (for the metal) to fcc (for the hydride), and the embrittlement of the ductile parent metals because of hydrogen damage.²⁶ The penetration of hydrogen into the metallic structure of Ti induces changes in the band-structure such as the appearance of a wide metal-hydrogen bonding band centered about 5.5 eV below the Fermi level E_F , the states near E_F are primarily metal d -derived.²⁶

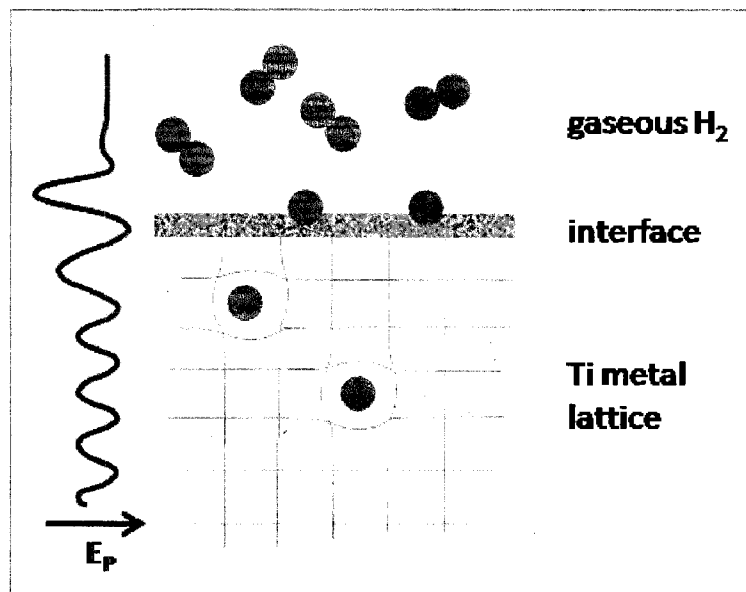


Figure 1. Simple model of the process of dissociation of molecular hydrogen at the interface with a metal such as titanium. The potential energy is characterized by first the shallow minimum corresponding to physisorption (Van der Waals - weak intermolecular interactions) then the deepest minimum corresponding to chemisorption (the formation of a chemical bond), the near surface hydrogen (second deep minimum) and finally H dissolved on interstitial sites of the host metal (periodic minima). (Drawing after Schlapbach¹²).

How does hydrogen interact with the surfaces of solid titanium metal? When the H_2 approaches the metal surfaces, it is dissociated on and then absorbed into the surfaces. The process of how hydrogen gas penetrates a dissolving metal is often represented with the schematic of Figure 1.

The difference in energy barrier for the dissociation of H_2 on the surface of a metal depends on the valence electron configurations of the substrate atom.¹² Theoretical studies²⁷ have shown that for metals such as Ti, Ni, Pd and La, the dissociative energy barriers are very small. In the case of Mg, a high energy barrier exists, which is why a catalyst is needed to lower it. As a H_2 molecule approaches the metal surface, its molecular orbitals begin to overlap with the surface s-electrons.^{12, 27} Because of the Pauli exclusion principle, if a metal atom has its valence electron states fully occupied, the electrons of H_2 are repelled and the outcome is a high H_2 dissociation barrier. On the other hand if a metal has a partially unoccupied d-orbital then electrons can be donated from the H_2 s-orbital to the surface metal atoms. This process happens along with a back-donation from the metal d-orbitals to the H_2 anti-bonding state.^{12, 27} The end result is that the interaction of the d-orbital valence electrons of the surface of the metal enhances the H_2 dissociation. In the case of Ti where the valence electron configuration is $4s^2 3d^2$, the d-orbital is almost empty, which results in a negligible H_2 dissociation energy barrier. The formation of TiH_2 is exothermic like that of the other hydrides of the IVA group.¹⁰

2.3.2. Catalytic Action of TiH_2

Titanium hydride can act as a catalyst in many reactions. Some examples include the organic hydrogenation reactions of olefins, nitro compounds and nitriles to amines.^{10, 11} Another potentially interesting catalytic action is in the hydrogenation of materials of which could be used for storing hydrogen.

An important issue of using metal hydrides for storing hydrogen for use in fuel cells is the hydrogen uptake kinetics. Hydrogen absorption in metal hydrides involves two main steps⁸: dissociation of the hydrogen molecule and transport of the chemisorbed hydrogen toward the subsurface and adjacent diffusion in the bulk (see Fig. 1). According to diffusion data, hydrogen transport inside metals or metal hydrides is fast enough to provide high hydrogen absorption and desorption rates at room temperature. However, in most systems only slow rates are observed, which is one clue that the surface properties of the metal grains determine their H sorption kinetics, that is, the dissociation of the hydrogen molecule.

Several empirical studies have advanced the possibility of enhancing hydrogen uptake kinetics by special additives (catalysts) to the metal hydride system. For instance, the kinetics of hydrogen sorption in Mg-based storage devices is greatly enhanced by such additives as transition metal oxides⁸ or TiH_x ¹⁷ and without a Ti catalyst, reversible hydrogen sorption is impossible in alanates.²⁸ A switchable mirror effect was recently observed in the Mg plus Ti system with reversible formation of MgH_2 . The observed decrease in reflectance was from ~65 % (between 500 and 2500 nm) for the metallic state down to about 10 % for the hydride state. Ti acted primarily as a catalyst for the

formation of MgH_2 .²⁹ Catalysis is now a broadly recognized as a critical issue in hydrogen production, storage, and use.¹ Catalysts also play a critical role in improving the kinetics and thermodynamics in hydrogen storage systems, allowing more efficient uptake and release of stored hydrogen with reduced need for thermal activation.^{6, 7, 30}

2.4. The Structures of Crystals

A crystal is an assembly of regularly repeating atoms, molecules or groups of atoms.³¹⁻³³ The pattern formed by points where the atoms (or molecules) are located is called a space lattice. In this sense the space lattice can be viewed as an abstract scaffolding of the crystal structure where atoms or groups of atoms are placed at the specific locations of the lattice points. The atoms can be placed centered on the lattice points or at a specific location with respect to the lattice points. The crystal is constructed by repeating by (3D) translation (no rotations, inversions or reflections) of one fundamental region: the unit cell. The unit cell is chosen not to be the absolute smallest repeatable motif in a structure, but to be the smallest motif containing the most symmetry. It should be noted here that the absolute smallest motif that can be repeated in order to build a structure is called an asymmetric unit.³⁴ The asymmetric unit may or may not coincide with the unit cell. The unit cell is an imaginary parallelepiped formed by joining neighboring lattice points by straight lines, and its three dimensions are labeled a , b and c . The unit cell is chosen so that it has the shortest sides and most nearly perpendicular faces. There are two types of unit cells: primitive cells have lattice points at the corners of the unit cell while a non-primitive unit cell has

also lattice points at either the centers of all faces or at centers of pairs of opposite faces or at the center of the body. Unit cells are further organized according to essential rotational symmetry elements which can be distinguished in them, what results in seven crystal systems: cubic (four C_3 axis), hexagonal, tetragonal (one C_4 axis), rhombohedral, orthorhombic, monoclinic, triclinic (no rotational symmetry). The rhombohedral system can be considered as part of the hexagonal system so the number may then be reduced to six crystal systems. Combining the seven crystal systems with the primitive and non-primitive unit cells yields the crystal lattices. But not all combinations exist and there are in fact only 14 crystal lattices called Bravais lattices, named after named after Auguste Bravais, a French physicist who in 1845 pointed out that there were only 14 instead of the previously thought 15 lattices in three dimensional crystal systems. If we distinguish lattices further by their symmetry elements - identity, n -fold rotation, reflection m , inversion, n -fold improper rotation – then we have 34 point groups or crystal classes. By adding translation to the set of symmetry elements we obtain 230 space groups: 2 triclinic structures (#1-#2), 13 monoclinic structures (#3-#15), 59 orthorhombic structures (#16-#74), 68 tetragonal structures (#75-#142), 25 trigonal structures (#143-#167), 27 hexagonal structures (#168-#194), 36 cubic structures (#195-#230).³¹⁻³³

In a crystal the spacing of lattice planes, whether of identical or of different atoms is an important quantitative aspect of the structure. A crystal lattice plane is labeled by three numbers, called Miller indices and denoted (hkl) 's, which are the reciprocals of the distances at which this plane intersects the a -, b - and c -axes, respectively. The Miller indices are multiplied by a common factor to eliminate fractions

so that the (hkl) 's are integers. In this way when a plane lies along an axis, the intersection lies at infinity, its reciprocal is one over infinity or zero. Also the smaller the value of an index, the more parallel the plane is to the corresponding axis ($h \rightarrow a$, $k \rightarrow b$, $l \rightarrow c$). Miller indices are used in expressing the separation of planes d in a crystal system. For example in an orthorhombic crystal system the relationship between d and (hkl) s is:

$$\frac{1}{d_{hkl}^2} = \frac{h^2}{a^2} + \frac{k^2}{b^2} + \frac{l^2}{c^2}$$

2.5. Overview of X-Ray Diffraction

With today's state of the art high-resolution electron microscopes or a tunnel microscope atomic structures of crystals can be imaged directly, and it appears as such microscopes could supplant the "antiquated" idea of indirect imaging through diffraction.³² In reality, however, diffraction yields more information regarding an unknown structure or structural parameters because it is optimally sensitive to the periodic nature of the crystal. On the other hand sophisticated direct imaging techniques are ideally suited for the study of any disruption of periodicity such as point defects, surfaces and interfaces. Diffraction experiments can be carried out using X-rays, neutrons for the bulk and electrons and atoms –primarily for the surface - all of which have different (elastic or inelastic) interactions with a solid. Diffraction can be described quasi-classically since the only quantum mechanical idea is that a beam of X-rays or neutrons possesses the wave-particle dual nature.³²

Diffraction is the constructive and destructive interference of radiation caused by an object in the path of the radiation and of size comparable to the wavelength of

radiation.³¹⁻³³ Since the intensity of electromagnetic radiation is proportional to the square of the amplitude of the waves, regions of constructive interference appear as having an enhanced intensity. The spacing of atoms in a crystal is on the order of one to a few Å, therefore the appropriate wavelength to study their structure through diffraction falls in the X-ray region. X-rays range from “soft” just above the Carbon K edge to hard X-rays in the 100 keV range. These limits, however, are not very well defined and differ slightly depending on the scientific community.³⁵ The most common X-ray radiation wavelengths used are those of CuK_α (1.54056 Å) as well as the sub-angstrom wavelengths of synchrotron radiation. The depth of penetration of an x-ray beam depends on the solid and on the photon energy but a typical depth is about 1 cm.³¹

2.5.1 Production of X-rays

In the laboratory, X-rays are generated by accelerating electrons through a potential difference, and bombarding a metal target with these high-energy electrons (~keVs).³⁶ Typical anode materials in X-ray tubes are: chromium, iron, cobalt, nickel, copper, molybdenum, silver and tungsten.³⁷ The collision with a metal target decelerates the electrons and the difference in energy is emitted as a continuous range of wavelengths, or Bremsstrahlung radiation. If some electrons have just the right amount of energy for ionization, they will collide and remove an electron from the K-shell of the target metal. The thus created vacancy will be immediately filled by an electron from the L or M-shell. (It is also possible, but less probable, that the vacancy will be filled with an electron from outside of the atom.) As the electron falls into a

lower energy shell it will emit the excess energy as an X-ray photon called K_α and K_β radiation, depending on whether it originates from the L- or the M-shells, respectively. The radiation will be in the X-ray range because the energy difference between the L and K-shells in a high-Z metal is of several thousands of keVs.³⁶ Vacancies are also created in higher shells (M, N and up) but the energy differences between the levels are much smaller and the emitted radiation appears as part of the continuous radiation (Bremsstrahlung).

2.5.2. The Bragg Equation

The foundation of almost all modern crystallography lies in the work of William Henry Bragg and his son William Lawrence Bragg which took place in 1913 and brought the pair a Nobel prize almost instantly, in 1915.³⁶ Let's consider the crystal to be a set of parallel lattice planes separated by a distance d , and acting like a mirror for incoming X-rays (Figure 2). It is then straightforward to derive the condition on the angle between the lattice plane and the incident X-rays necessary for constructive interference. The difference of the length of the path of two X-rays diffracting from two planes separated by d must be an entire number of wavelengths λ . The condition on the path difference is called the Bragg law and is:

$$n\lambda = 2 d \sin\theta$$

Here n indicated the order of the reflection (or intense beam arising from constructive interference). In modern X-ray diffraction n is combined with d and hence the n^{th} order reflection is considered as originating from the $(nh \ nk \ nl)$ plane.

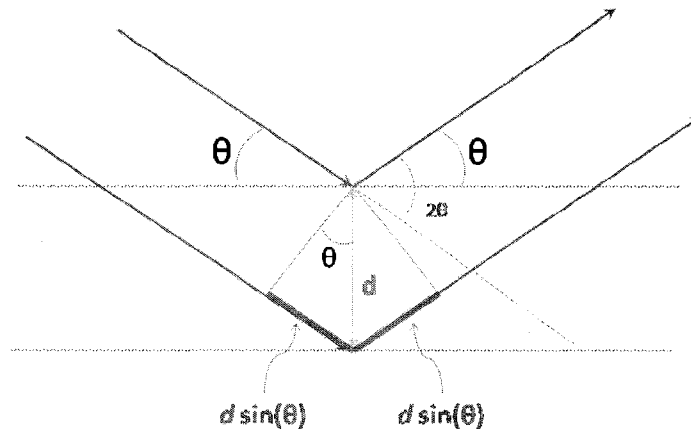


Figure 2. Schematic illustrating the principle of Bragg's law. In order for the two waves to be in phase after they reflect from the two parallel planes, the path difference between the two waves must be equal to an integer number of wavelengths.

For a known angle, the d -spacing of a set of planes may be calculated. Once d is known then if the reflections can be indexed - that is ascribed (hkl) values - then one can obtain the lattice parameters a , b , and c of the unit cell. The key to solving a structure is then indexing.³² Once the crystal structure is known, the parameters describing it, such as atom position and unit cell dimensions are adjusted (Rietveld refinement) until the calculated pattern (from the model of the structure) matches best the experimental pattern.³² This can often be problematic for low symmetry system with a lot of reflections and for cases where there is more than one probable structure that differ very little. Finally, the next major step after refinement of the structure at ambient pressure is uncovering of possible phase transitions and the structural refinement when

the pressure variable is introduced in the experiment. Such is the procedure followed in the presented work.

2.5.3. The Laue Method

William Bragg and his son Lawrence Bragg used a monochromatic X-ray beam and varied the angles of a single crystal to detect the possible reflections. Max Von Laue considered that for one wavelength, a single crystal may not have the right orientation.³³ However, if a range of wavelengths was shone through a crystal there would be at least one plane that would have the right orientation to satisfy the Bragg condition. Hence, the Laue method employs a beam of X-rays with many wavelengths and, if the range of wavelengths is wide enough, then there will be an appropriate wavelength for each plane in the single crystal. The resulting diffraction pattern, projected on a flat surface (detector) is a set of geometrically spaced dots. The Laue method is used today at synchrotron beamlines with polychromatic beams.

2.5.4. The Debye-Scherrer Method

If a monochromatic beam is used with a polycrystalline sample where there are a lot of crystals with random orientation, then the Bragg condition will be satisfied as well. This technique was developed by Peter Debye and Paul Scherrer and by Albert Hull independently, and it is called the Debye-Scherrer method.³³ Let's consider a given set of planes denoted by (hkl) 's and located in crystals which have a random orientation in the powder sample. For a specific angle ϑ there will be crystallites with the right orientation of that plane as to satisfy the Bragg angle all around the X-ray beam. Therefore, constructive interference will give rise to a reflection all around the beam in

the form of a cone of light of internal angle 2θ diverging from the sample. Initially such cones of light were detected by placing a strip of photographic film around the sample so that the sample would be at the center of the circle. This detection method allowed to measure the angle of the reflections. One could also make qualitative and quantitative observations of the intensities. Nowadays detectors have various geometries (image plates, rotating detectors) and they can measure the intensities of the reflections quantitatively.

2.6. Theory of X-Ray Diffraction

W. L. Bragg's explanation for the diffracted beams from a periodic crystal structure assumed a mirror like behavior of the material. The Bragg equation is beautiful in its simplicity however it is convincing only³¹ because it reproduces the correct result. Below is a more rigorous derivation of the condition of diffraction.^{31,32}

In order to describe diffraction one must start from a few basic assumptions. One assumption is that an incoming wave of X-rays, for example, will undergo single scattering and thus emit spherical waves from all points of an atom. If the waves are being emitted from a sufficiently distant source, they can be considered as plane waves at the site of an atom of the considered solid. Also we need to assume coherent scattering – a fixed phase between the incoming wave and the scattered spherical waves. Let the scattering center be located at a point P and the observation point to be labeled B (see Figure 3.1). The amplitude of X-rays at point P can be expressed as:

$$A_P = A_0 e^{i\vec{k}_0 \cdot (\vec{R} + \vec{r}) - i\omega t}$$

After scattering occurs, spherical waves are emitted from the sample and their amplitude and phase relative to the incident wave are described by the complex scattering density $\rho(r)$. At the detection point B the spherical waves can be therefore expressed as:

$$A_B(r, t) = A_P \rho(\vec{r}) \frac{e^{ik|\vec{R}' - \vec{r}|}}{|\vec{R}' - \vec{r}|}$$

And since the vector \vec{k} is in the direction of $\vec{R}' - \vec{r}$ and further $R' \gg r$:

$$A_B(r, t) = A_P \rho(\vec{r}) \frac{e^{i\vec{k} \cdot (\vec{R}' - \vec{r})}}{R'} = \frac{A_o}{R'} e^{i(\vec{k}_o \cdot \vec{R} + \vec{k} \cdot \vec{R}')} e^{-i\omega_o t} \rho(\vec{r}) e^{i(\vec{k}_o - \vec{k}) \cdot \vec{r}}$$

In order to obtain the total scattering amplitude one must integrate over the entire scattering region:

$$A_B^{total}(t) \propto e^{-i\omega_o t} \int \rho(\vec{r}) e^{i(\vec{k}_o - \vec{k}) \cdot \vec{r}} d\vec{r}$$

Since in diffraction we measure the intensity of the scattered waves and the intensity being proportional to the square of the amplitude we have:

$$I(\vec{K}) \propto |A_B^{total}(t)|^2 \propto \left| \int \rho(\vec{r}) e^{i(\vec{k}_o - \vec{k}) \cdot \vec{r}} d\vec{r} \right|^2$$

Where the scattering vector is defined as: $\vec{K} = \vec{k} - \vec{k}_o$

2.6.1. The Reciprocal Space

If we consider a crystal, which is a structure with translational symmetry, its electron density is periodic, so $\rho(\mathbf{x}) = \rho(\mathbf{x} + n\mathbf{a})$ where $n=0, 1, 2, \dots$ and a is the lattice parameter (in 1D).^{31, 32} Expanding in a Fourier series we have:

$$\rho(x) = \sum_n \rho_n e^{i\left(\frac{2\pi n}{a}\right)x}$$

In 3D the position \vec{r} is described by three lattice vectors

$$\vec{r}_n = n_1 \vec{a}_1 + n_2 \vec{a}_2 + n_3 \vec{a}_3$$

Then the electron density in 3D is written:

$$\rho(\vec{r}) = \sum_{\vec{G}} \rho_{\vec{G}} e^{i\vec{G} \cdot \vec{r}}$$

where the vector \vec{G} is defined with basis vectors and intereger multipliers:

$$\vec{G} = h\vec{g}_1 + k\vec{g}_2 + l\vec{g}_3$$

In order for electron density to remain a periodic function, we need to impose a set of conditions on the vector \vec{G} :

$$\vec{G} \cdot \vec{r}_n = 2\pi m$$

For example if $n_2=n_3=0$ then $(h\vec{g}_1 + k\vec{g}_2 + l\vec{g}_3) \cdot n_1 \vec{a}_1 = 2\pi m$, which can be insured if $\vec{g}_1 \cdot \vec{a}_1 = 2\pi$ and $\vec{g}_2 \cdot \vec{a}_1 = 0$ and $\vec{g}_3 \cdot \vec{a}_1 = 0$ which is equivalent to writing:

$$\vec{g}_i \cdot \vec{a}_j = 2\pi \delta_{ij}$$

The three \vec{g}_i vectors span the reciprocal space and the three values h , k and l are the reciprocals of points where the plane intersects the a , b , and c axis of the unit cell, respectively. The above equation indicates that, for example, vector \vec{g}_1 is perpendicular to \vec{a}_2 and \vec{a}_3 (and hence to the plane formed by them), and that its length is $2\pi/(a \cos \varphi)$ where φ is the angle between \vec{g}_1 and \vec{a}_1 . This can also be expressed by:

$$\vec{g}_1 = 2\pi \frac{\vec{a}_2 \times \vec{a}_3}{\vec{a}_1 \cdot (\vec{a}_2 \times \vec{a}_3)}$$

where the other vectors can be obtained by cyclic permutation.

2.6.2. The Laue condition

Let's return to $I(\vec{K}) \propto \left| \int \rho(\vec{r}) e^{i(\vec{k}_o - \vec{k}) \cdot \vec{r}} d\vec{r} \right|^2$ and insert the expression for

$$\rho(\vec{r}) = \sum_{\vec{G}} \rho_{\vec{G}} e^{i\vec{G} \cdot \vec{r}} :$$

$$I(\vec{K}) \propto \frac{|A_o|^2}{R'^2} \left| \sum_{\vec{G}} \rho_{\vec{G}} \int e^{i(\vec{G} - \vec{K}) \cdot \vec{r}} d\vec{r} \right|.$$

It can be shown that, in fact, the above sum is negligibly small when \vec{K} differs significantly from \vec{G} . If the integral was expressed in components then for an infinite volume it would be a representation of respective δ -functions. We then have:

$$\int e^{i(\vec{G} - \vec{K}) \cdot \vec{r}} d\vec{r} = \begin{cases} \text{the scattering volume } V \text{ for } \vec{G} = \vec{K} \\ \sim 0 \text{ otherwise} \end{cases}$$

The Laue condition ^{31, 32} states that scattering from periodic structures will lead to diffraction if the difference between the \vec{k} vectors of scattered and incident wave corresponds to \vec{G} (Figure 3) or:

$$\vec{G} = \vec{K}$$

Then the intensity that can be measured in a diffraction experiments is:

$$I_{\text{measured}}(\vec{K} = \vec{G}) \propto \frac{|A_o|^2}{R'^2} |\rho_{\vec{G}}|^2 V^2$$

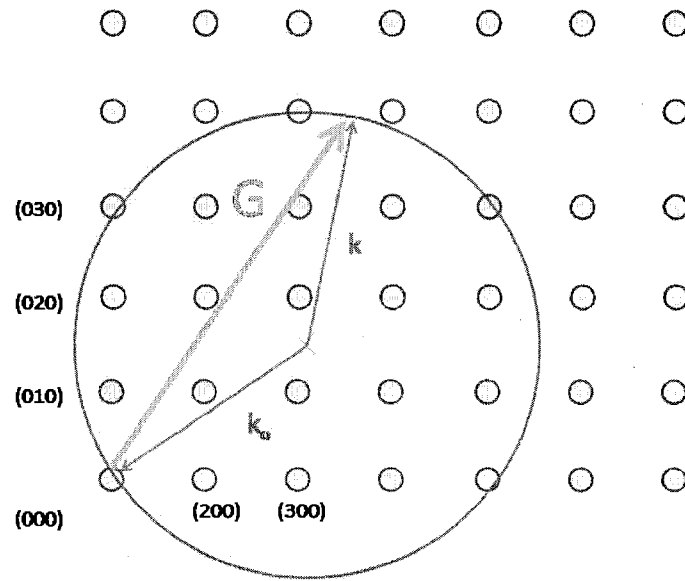


Figure 3. Schematic of a reciprocal lattice with (hkl) 's marking some of the reciprocal planes. The (reciprocal) c axis points out of the page. The circle represents the Ewald sphere of the reciprocal lattice illustrating the Laue condition $\vec{G} = \vec{K} = \vec{k} - \vec{k}_0$. A diffracted beam will be produced whenever a reciprocal lattice point coincides with the surface of the sphere.

The vector \vec{G} is uniquely defined in the basis \vec{g}_i of the reciprocal lattice by its three coordinates h , k and l . These indices can also be used to label the diffraction beams or reflections since a specific plane has a unique set of coordinates and it gives rise to one reflection which appears a peak in the diffraction pattern (Fig. 3).

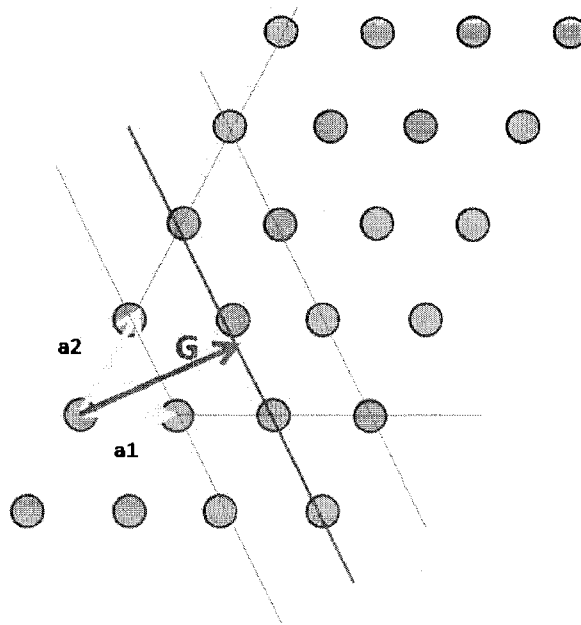


Figure 4. Set of crystal lattice plains in real space. The plane in red intersects the axis at $(2, 2, \infty)$ so the plane's (hkl) 's are $2 \cdot (1/2, 1/2, 0)$ which is (110) . All planes parallel to this plane are equivalent, because they contain the same density of atoms.

Let's consider one lattice plane in a periodic crystal structure: we can label the three points where the plane intersects with the coordinate axis as m , n and o and call the reciprocals of these numbers $h'=1/m$, $k'=1/n$ and $l'=1/o$ (Figure 4). In order to avoid dealing with fractions one can multiply h' , k' and l' by an integer p and obtain a set of three integers: h , k , l which are the coordinates of G . A given \vec{G}_{hkl} is perpendicular to the corresponding (hkl) plane (Fig. 4).

2.6.3. The Bragg Equation

The distance from the origin of the lattice to a (hkl) plane is:

$$d'_{hkl} = \frac{a_1}{h'} \cos(\varphi) = \frac{a_1}{h'} \left(\frac{\vec{a}_1 \cdot \vec{G}_{hkl}}{a_1 G_{hkl}} \right) = \frac{1}{h'} \frac{2\pi h}{G_{hkl}} = \frac{2\pi}{G_{hkl}} \frac{h}{h'} = \frac{2\pi}{G_{hkl}} p$$

The distance to the nearest plane is then:

$$d_{hkl} = \frac{d'_{hkl}}{p} = \frac{2\pi}{G_{hkl}}$$

The Laue condition is the condition for scattering so one should be able to obtain the Bragg equation from it:

$$|\vec{G}| = |\vec{k} - \vec{k}_o|$$

$$G_{hkl} = \frac{2\pi}{d_{hkl}} = 2k_o \sin \theta$$

$$\frac{2\pi}{d_{hkl}} = 2 \frac{2\pi}{\lambda} \sin \theta$$

$$\lambda = 2d_{hkl} \sin \theta$$

In this way we obtain the Bragg equation,^{31, 32} which says that the path difference between waves scattering from two parallel adjacent planes should be equal to the wavelength (or an integer of wavelengths) in order to produce constructive interference and hence a reflection.

2.6.4. Atomic scattering factor

How much of incoming X-rays will be scattered by an atom, that is the intensity of a reflection, depends on the electron density or in equation form: $I_{hkl} \propto |\rho_{hkl}|^2$ where $(\vec{r}) = \sum_{\vec{G}} \rho_{\vec{G}} e^{i\vec{G} \cdot \vec{r}}$. The coefficients of the Fourier series of the scattering density are:

$$\rho_{hkl} = \frac{1}{V_c} \int_{\text{unit cell}} \rho(\vec{r}) e^{-i\vec{G} \cdot \vec{r}} d\vec{r}$$

In an element, the core electrons are concentrated in a small region around the atom (except for light elements, which are also ones that are least appropriate for investigation by X-rays). In comparison to core electrons, scattering from valence electrons is negligible. So we can consider the total scattering density of a crystal lattice as a sum of scattering densities of component atoms. Let \vec{r}_n be the origin of the n^{th} unit cell, \vec{r}_α be the position of of each atom in the unit cell and \vec{r}' be a position vector pointing away from the center of each atom (Figure 5) so that $\vec{r} = \vec{r}_n + \vec{r}_\alpha + \vec{r}'$.

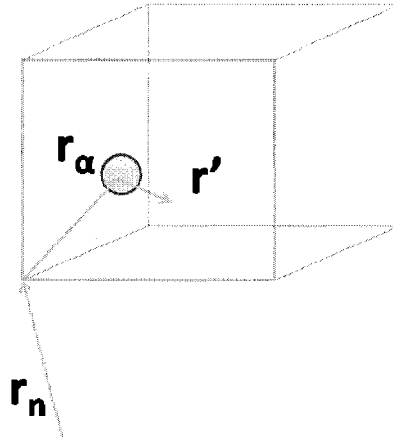


Figure 5. Schematic illustrating the decomposition of the position vector \vec{r} into three vectors where $\vec{r} = \vec{r}_n + \vec{r}_\alpha + \vec{r}'$. The box represents a unit cell from a crystal lattice.

Then the scattering density of a single atom is:

$$\rho_{hkl}^{single\ atom} = \frac{1}{V_c} \sum_{\alpha} e^{-i\vec{G} \cdot \vec{r}_{\alpha}} \int_{\alpha} \rho_{\alpha}(\vec{r}') e^{-i\vec{G} \cdot \vec{r}'} d\vec{r}'$$

where we can define the atomic scattering factor or form factor (De):

$$f_{\alpha} = \int_{\alpha} \rho_{\alpha}(\vec{r}') e^{-i\vec{G} \cdot \vec{r}'} d\vec{r}'$$

Switching from Cartesian to polar coordinates:

$$f_{\alpha} = \int_{\alpha} \rho_{\alpha}(\vec{r}') e^{-i\vec{G} \cdot \vec{r}'} d\vec{r}' = - \iiint \rho_{\alpha}(r') e^{-iGr' \cos \theta} r'^2 dr' \sin \theta d\varphi$$

$$f_{\alpha} = 4\pi \int \rho_{\alpha}(r') r'^2 \frac{\sin(Gr')}{Gr'} dr'$$

Now since the diffraction angle between \vec{k} and \vec{k}_o is 2θ , the using Eq. 24 we have the final definition of atomic scattering factor or form factor:

$$f_{\alpha} = 4\pi \int \rho_{\alpha}(r') r'^2 \frac{\sin [4\pi r' \sin(\frac{\theta}{\lambda})]}{4\pi r' \sin(\frac{\theta}{\lambda})} dr'$$

The maximum of the atomic scattering factor occurs for $\theta=0$ where the integral becomes equal to the scattering density, which in turn is proportional to the total number of electrons per atom.

2.6.5. Structure Factor

If we consider again all the atoms of a unit cell then we arrive at the definition of the structure factor:

$$F_{hkl} = \sum_{\alpha} f_{\alpha} e^{-i\vec{G}_{hkl} \cdot \vec{r}_{\alpha}}$$

where the summation is over the atoms in the unit cell (see Fig. 5). So finally the scattering density is expressed as:

$$\rho_{hkl}^{single\ atom} = \frac{S_{hkl}}{V_c}$$

The intensity of diffraction lines is proportional to the square of the wave amplitude or of the structure factor:

$$I_{hkl} \propto F_{hkl}^* F_{hkl}$$

And if we consider for example that there are two different atoms in the unit cell then we have:

$$\begin{aligned} I_{hkl} \propto F_{hkl}^* F_{hkl} &= \left(f_1 e^{-i\vec{G}_{hkl} \cdot \vec{r}_1} + f_2 e^{-i\vec{G}_{hkl} \cdot \vec{r}_2} \right)^* \left(f_1 e^{-i\vec{G}_{hkl} \cdot \vec{r}_1} + f_2 e^{-i\vec{G}_{hkl} \cdot \vec{r}_2} \right) \\ &= \left(f_1 e^{+i\vec{G}_{hkl} \cdot \vec{r}_1} + f_2 e^{+i\vec{G}_{hkl} \cdot \vec{r}_2} \right) \left(f_1 e^{-i\vec{G}_{hkl} \cdot \vec{r}_1} + f_2 e^{-i\vec{G}_{hkl} \cdot \vec{r}_2} \right) \\ &= f_1^2 + f_1 f_2 \left(e^{+i\vec{G}_{hkl} \cdot \vec{r}_1 - i\vec{G}_{hkl} \cdot \vec{r}_2} + e^{+i\vec{G}_{hkl} \cdot \vec{r}_2 - i\vec{G}_{hkl} \cdot \vec{r}_1} \right) + f_2^2 \\ &= f_1^2 + f_2^2 + 2f_1 f_2 \cos(\phi_{hkl}) \end{aligned}$$

Finally we have a simple expression for the intensity of diffracted X-rays:

$$I_{hkl} \propto F_{hkl}^* F_{hkl} = f_1^2 + f_2^2 + 2f_1 f_2 \cos(\phi_{hkl})$$

The intensities of reflections are altered by the presence of other atoms in the cell and this can sometimes lead to characteristic extinctions of certain reflections (if two different atoms have the same Z and their scattered waves are 180° out of phase).

In conclusion the Bragg reflections' positions provide information about the shape and the dimensions of the unit cell, whereas the intensities of those reflections yield insight into the type of atoms present in the unit cell.

When it is desired to investigate the structure of a solid on the atomic scale then the wavelength used should be at least on the order of the lattice constant. We can only measure the intensity of the diffracted radiation, so we do not obtain any information about phases. If one could actually measure the amplitude of the scattering radiation, then the scattering density could be obtained by inverse Fourier transform of the amplitude. The lack of information about phases leads to the necessity of trying out different model structures (and varying their parameters which can be extremely time-intensive) and determining which one fits the best the experimental diffraction pattern.

2.6.6. Temperature Factor

The Debye-Waller factor (DWF), named after Peter Debye and Ivar Waller, is used to describe the attenuation of X-ray scattering (and also neutron) scattering caused by thermal motion or quenched disorder. It gives the fraction of elastic scattering. Assuming a solid is a classical harmonic oscillator the Debye-Waller factor is given by the exponential factor in the expression:

$$I(hkl) = I_o e^{\left(-\frac{1}{3}\langle u^2 \rangle G^2\right)} = I_o e^{\left(-\frac{k_B T G^2}{M \omega^2}\right)}$$

where $\langle u^2 \rangle$ is the mean square displacement of an atom, M is the mass of the atom, ω is the frequency of the oscillator.³¹ This classical result approximates well experimental data at high temperatures. At low temperatures one must use quantum considerations. At $T=0$, the is the mean square displacement $\langle u^2 \rangle$ of an atom does not vanish because of zero point motion, and the scattered intensity is:

$$I(hkl) = I_0 e^{\left(-\frac{\hbar G^2}{2M\omega}\right)}$$

which gives about 90% of elastic scattering when typical numbers are substituted.³⁸

The Debye-Waller factor was first called the temperature factor because Peter Debye (1913) and Ivar Waller (1923) were the first to understand and formulate the effect that thermal vibrations would have on the intensity of X-ray scattering. Since then it has become obvious that static displacements produce a similar effect on the scattered intensities of X-rays therefore the use of the term 'temperature factor' is formally discouraged, as stated by the 1996 IUCR Commission on Crystallographic Nomenclature.³⁸ What are the key components of static displacement? First is the displacement arising from atomic vibrations because of motion of molecules or molecular fragments or, in a crystal, because of internal vibrations, such as bond stretching and bending. All of these motions are temperature-dependent, unless the temperature is very low. Besides temperature effects there are other effective displacements from the mean position which are because of a variety of possible types of disorder. Disorder includes small deviations from ideal periodicity, present in all real crystals; orientational disorder, present in many molecular crystals; density and displacement modulations; and short- and long-range displacive correlations. Besides decreasing the intensity of diffraction lines, many types of disorder also give rise to diffuse scattering.

2.7. High-Pressure in Materials Science

2.7.1. Introduction

Pressure and temperature are the key parameters in the thermodynamic study of materials. Materials at high-pressures are found in nature in oceans (0.1 GPa) and inside the Earth (center at 360 GPa) as well as within planets, stars, and the universe.³⁹ The static high-pressure range in nature and in the universe spans about 130 orders of magnitude and is hence larger than for any other physical variable.⁵ Nowadays, pressures superior to those found at the center of the earth can be replicated in the laboratory environment. The pressure variable can be applied in a very controlled manner to samples of the order of few microns to a few centimeters cubed, by using either a diamond anvil cell or for the latter, a large volume press.

A wealth of information can be obtained when molecular materials are subjected to very high-pressures. In fact, pressure allows for tuning of electronic, magnetic, structural and vibrational properties. Another application in fundamental science is the possibility to tune interatomic bonds for the purpose of testing theories.³⁹

In summary, high-pressure research enables a better understanding of structural properties of materials, of chemical reactions, and of materials synthesis. Phase transitions, phase diagrams and equations of state have been determined for countless systems with the use of pressure and temperature combined with *in situ* X-ray diffraction.⁴⁰

2.7.2. The Progress and Diversification of High-Pressure Research

High-pressure diffraction has been carried out for over 40 years now. Synchrotron sources, pressure cells and data acquisition and analysis systems are incessantly being modified and improved in the search for better, faster and more efficient experiments.⁴⁰ Synchrotron radiation was used for the first time in combination with X-ray diffraction 30 years ago, in 1977.⁴¹ High-pressure X-ray diffraction studies involving synchrotron radiation were first reported in 1977 as well.⁴¹ The key advantages of synchrotron X-rays, as applied to high-pressure studies, were the tunable wavelength, improved resolution, low noise and excellent statistics. On the other hand, high-pressure created new constraints because of the extremely small sample size and absorption and scattering due to small angular range.

High-pressure techniques have been steadily advancing since the eighties, with development accelerating in the past few years. Accompanied by the parallel development in new synchrotron techniques (diffraction, spectroscopy, from X-ray to infrared region) all these developments allowed high-pressure research to flourish into an interdisciplinary tool spanning geosciences, different domains of physics, materials science and even biology.

High-pressure research has known an unprecedented wave of growth across research areas in the last 20 years.³⁹ The developments that contributed to making high-pressure the thriving research field it is today, are the evolution of diamond anvil cells and the arrival of 3rd generation synchrotron sources with the parallel advances in

synchrotron techniques. Today the pressure limit achievable in the laboratory is ~5 Mbars.

2.7.3. The Effect of Pressure on Matter

What is the effect of pressure ^{4, 39} on a solid? As interatomic distances are reduced under pressure, the material becomes denser. It is then relevant to examine what are the mechanisms for increasing the density of a material. As the crystal lattice is reduced and atoms are drawn closer, compression acts on the energetics of electrons. The energy of electrons is composed of kinetic, coulomb, exchange and correlation contributions. From the point of view of density functional theory, the kinetic energy of electrons is proportional to electron density to the 5/3 power. Therefore, the kinetic energy increases fast under compression. ⁴ Electrons tend towards states of lower kinetic energy. As a consequence intramolecular bonds are destabilized. Already in the 1930s it was postulated that at pressures sufficiently high molecular systems will transition to close-packed structures before, or in concert with, the formation of a fully metallic phase (“metallic or valence states”) ⁴² and ultimately form a plasma in which the chemical description of bonding does not hold anymore. In fact, as atoms are brought together, changes in hybridization occur, because of covalent interactions. On compression it is possible for different types of bonds (van der Waals, ionic, covalent, metallic and hydrogen) to compete among each other.

Since it is possible to achieve, in the laboratory, pressures high enough to reduce the unit cell volume by more than a factor of 2, the resulting changes in inter-atomic bonding can be immense and hence the properties of high-pressure phases can differ

greatly from the ambient pressure and temperature phase.³⁹ As a result of compression the atomic arrangement can suddenly change. As the Gibbs free energy of different arrangements of atoms varies under pressure, it may become more energetically favorable for the material to change this arrangement in which case a solid-solid phase transition occurs. This change in atomic arrangement can either be discontinuous or continuous and accompanied by a change in crystal symmetry.

Under high-pressures some materials adopt high-symmetry structures of increasing coordination number. However, some materials can first transition into lower symmetry structures at intermediate pressures and only at higher pressures they transform into higher-symmetry structures.

So what is the bottom line result of compression? Unexpected, intermediate states can be formed at high-pressures as molecular bonds evolve before being annihilated. Pressure can induce autoionization as well as molecular bonding. New materials can be produced by chemical reactions or mechanisms very different from those at ambient conditions and their kinetics maybe either accelerated or slowed down depending on the activation volume. High-pressures can be used to produce materials with technological implications such as super hard materials, nonlinear optical materials or high temperature superconductors. Pressure can also induce loss of long-range order or material amorphization, where glassy materials can be obtained below their regular glass transition temperature.⁴

2.7.4. At the Heart of High-Pressure Research: the Diamond Anvil Cell

The reliable and controlled replication of high-pressures in the laboratory begins with “the Bridgman” era as referred to by Jayaraman.⁴³ From 1910 to 1950 P.W. Bridgman invented and developed the Bridgman anvil and the piston cylinder device for electrical resistance and compressibility measurements (up to 100 kbar = 10 GPa).

The diamond anvil cell (DAC) was first developed by Jamieson, Lawson, and Nachtrieb⁴⁴ and Weir et al.⁴⁵ The principle of operation of any high-pressure device is based on the fact that a large force F applied to a small area A generates a large pressure $p=F/A$ (Figure 6). The smaller the area, the large will be the pressure created on the sample. The limit is the deformation and eventual fracture of the diamond under very high loads. Diamond is ideal for high-pressure applications because it combines the highest bulk modulus and hardness among all known materials.

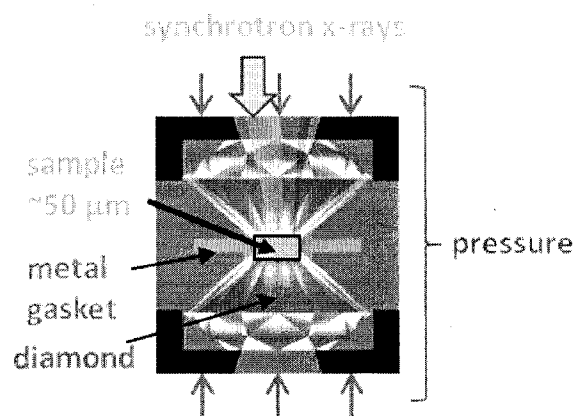


Figure 6. Schematic of the inside of a diamond anvil cell (DAC). Typical sizes are: 1/3 carat for the diamond with a culet of ~300 μm; the sample chamber is usually 100 μm or less.

In the DAC, a small amount of material is placed between the flat faces or culets of two diamonds.^{46, 47} The culets are separated by a thin metallic foil which serves as gasket. An initial compression of the gasket creates an indentation and a micron-size hole is drilled in the middle of the indentation. This hole constitutes the sample chamber where the desired sample is placed together with a pressure standard as well as a pressurizing fluid medium to insure (quasi-) hydrostaticity and homogeneous conditions. The diamond culets can have dimensions between 100 μm and 1000 μm , the metallic gasket has a thickness between 300 μm and as little as 100 μm (in the case of X-ray Raman) with the indented zone reduced to anywhere between 80 to 30 μm . The ideally circular hole centered in the indentation can have a diameter between 10 and 200 μm . Because of the small dimensions involved, as well as the need for perfect centering of various elements and high precision, all manipulations are carried out under a high-magnification optical microscope. The chief reason for using diamonds, besides their exceptional hardness, is also their wide window of optical transparency (except from $\sim 5.5\text{eV}$ to $\sim 15\text{ keV}$), up to hard X-rays which allows for a multitude of scattering and diffraction techniques. Diamond anvil cells have been the key limiting factor in high-pressure research.

2.7.5. How is Pressure Measured in a Diamond Anvil Cell?

Static pressure P is the force exerted per unit area. The force applied on a DAC is transmitted to the sample in a very complex way (especially above 10 GPa) because of the friction and deformation of the materials of the cell, so the generated pressure depends not only on the force but also on the mechanical properties of the materials.^{46,}

⁴⁷ In that case instead of modeling how pressure is transmitted to the sample chamber, it is much more practical to use transferable pressure scales. Here pressure measurements are based on the equation of state (P(V) isotherms) reference materials.

Primary pressure scales are based on materials such as Au, Pt, Ag, Cu or NaCl, for which the equations of state, which were established from a combination of ultrasonic data and shock-wave experiments, show a good degree of consistency to 100 GPa. In a typical X-ray diffraction compression experiment the lattice parameters of a primary pressure scale are accurately measured and the pressure is obtained through the corresponding equation of state.

Another possibility is the use of a secondary scale, calibrated against a primary pressure scale, and which may be easier to use in a high-pressure experiment. In fact, at very high-pressure, the accurate determination of the lattice parameters of a reference material becomes difficult. One such secondary scales is the very popular ruby ($\text{Al}_2\text{O}_3:\text{Cr}^{3+}$) scale, which has a fluorescence line (R_1) which shifts with pressure almost linearly up to 10 GPa, with $dp/d\lambda=0.2746 \text{ GPa } \text{\AA}^{-1}$, and with a small deviation at higher pressures, according to the empirical equation ⁴⁸ :

$$P(\text{GPa}) = \frac{1904}{B} \left[\left(1 + \frac{\Delta\lambda}{\lambda_o} \right)^B - 1 \right]$$

where $B=7.665$ for quasi-hydrostatic conditions and $B=5.0$ for non-hydrostatic conditions. The R_1 fluorescence line is also dependent on temperature with $d\lambda/dT=0.068 \text{ } \text{\AA} \text{ K}^{-1}$, so that an increase in temperature of 10 K corresponds to an increase in pressure of $0.187 \text{ GPa} \rightarrow 0.2 \text{ GPa}$.

$$0.2746 \text{ GPa } \text{\AA}^{-1} * 0.068 \text{ \AA K}^{-1} * 10 \text{ K} = 0.187 \text{ GPa}$$

In most of the presented studies in the experimental part of this Thesis both a primary and a secondary pressure scale was used.

2.8. Synchrotron X-Ray Diffraction

2.8.1. A Brief History of Synchrotrons

Synchrotron radiation got to a “poor” start at electron accelerators where it was seen as a nuisance since it represented loss of energy.^{35, 49} Materials scientists, who saw potential in synchrotron radiation, were sometimes allowed by particle physicists to tap into radiation that went lost otherwise and operate beam ports in “parasitic” mode. The first generation synchrotrons were born. From nuisance synchrotron radiation evolved to one of the most powerful tools for the study of matter. The next evolutionary step was the construction of what became known as the second generation synchrotron sources, of the 1980s. These were properly dedicated facilities and not merely attachments to particle accelerators. The second generation synchrotron sources were composed of two straight sections with a wiggler or an undulator and connected by two semi-circular ends with bending magnets.^{35, 49} Third generations sources, such as the Advanced Photon Source Argonne National Laboratory (Argonne, IL, USA), were built in the 1990s. They are composed of many straight sections connected in to a polygon and optimized to supply very bright radiation from far UV to hard X-rays depending on the synchrotron.

2.8.2. Productions of Synchrotron X-rays: Bending Magnets, Undulators

Synchrotron radiation goes from far infrared to hard X-rays. Highly parallel radiation originates from a very small source (0.01-0.1 mm in cross-section). It is linearly polarized in the plane of the electron orbit and elliptically polarized above and below the plane.

Accelerated charged particles emit radiation in the well known sine squared angular pattern of dipole radiation. The synchrotron makes use of the fact that centripetal acceleration of charged particles causes transverse emission of electromagnetic radiation in the tangential direction of the ring where electrons circulate (due to an applied magnetic field). If, in addition the particles travel at relativistic speeds, the radiation is emitted in a narrow cone, tangent to the path and in the forward direction, mimicking a sweeping searchlight or a train on a circular track.^{35,}

50

In a third generation synchrotron source the circular motion of a tightly confined beam of relativistic electrons is insured by bending magnets. End-stations that follow only a bending magnet are characterized by wide spectrum of radiation sometimes referred to as a synchrotron light bulb. Undulators can be found in straight sections between bending magnets and they are periodic magnetic structures with a large number of cycles (ex: 100). The relatively weak magnetic field of undulators causes the electrons to have a small harmonic oscillation which is also called undulation. The electrons experience additional acceleration in a direction which is perpendicular to their circular motion. Because of the fact that the amplitude of oscillation is small the

resultant radiation cone is narrow. Also since the original electron beam was already tightly confined, the end result is highly directional radiation with small angular divergence, small cross-section and narrow spectral width. The undulator radiation is quasi-monochromatic and approximates many of the desired properties of an X-ray laser. Wigglers are also periodic magnetic structures that can be found between bending magnets, but with fewer periods than undulators and with a much stronger magnetic field. Here the amplitude of oscillation is larger, and as the electron is jolted up and down, the resultant radiation cone is wider in space and angle. Stronger magnetic field also translates into larger radiated power. As a result the radiation from a wiggler has a wide spectrum much like for a bending magnet, but the spectrum is shifted towards higher energies and the photon flux is larger.^{35, 50}

Synchrotron radiation is the best tool for the study matter enclosed in a high-pressure cell. Synchrotron radiation is characterized by a very penetrating high-energy beam. High-brilliance and low-emittance of the beam permit to focus it down to micron sized spots, which are ideal when the sample chamber is itself a few tens of microns in diameter. The brilliance of X-rays at a third generation synchrotron source also reduces the data collection time down to a few minutes or a few seconds depending on the beamline versus hours or more for a standard X-ray diffractometer.^{35, 50}

2.8.3. The Advanced Photon Source at Argonne National Laboratory

There exists today only about a dozen of synchrotron facilities in the world that possess high-pressure-dedicated beamlines: APS (US), ESRF (FR), Spring-8 (JP), Soleil

(FR), NSLS (US), ALS (US), BSRL (China), HasyLab (DE), CHESS (US), KEK-PF (JP), SERC (UK), ELETTRA (IT), Australia, Korea).

The experimental work presented in this *Master of Science Thesis* was carried out at the U.S. Department of Energy's Advanced Photon Source of Argonne National Laboratory (Figure 7). Electrons are first emitted from a cathode ray tube and accelerated by high-voltage alternating electric fields in a linear accelerator. Selective phasing of the electric field accelerates the electrons to 450 MeV. At 450 MeV, (>99.999% of the speed of light). Electrons are injected into the booster synchrotron (a ring of electromagnets), and accelerated from 450 MeV to 7 GeV in one-half second (>99.999999% of the speed of light).⁵¹

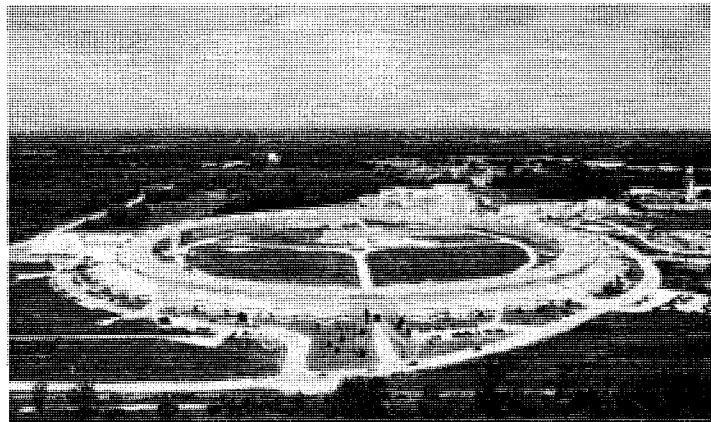


Figure 7. Aerial view of the Advanced Photon Source (APS), a third generation synchrotron, at Argonne National Lab. in Chicago, IL. (Picture courtesy of the APS-ANL⁵¹.)

The accelerating force is supplied by electrical fields in four radio frequency cavities. In order to maintain the orbital path of the electrons, bending and focusing magnets increase the electron field strength in synchronization with the radio frequency field. The 7-GeV electrons are injected into the 1104-m (3622 ft or ~0.7 mi) circumference storage ring, a circle of more than 1,000 electromagnets and associated equipment, located in a concrete enclosure inside the experimental hall. A powerful electromagnetic field focuses the electrons into a narrow beam that is bent on a circular path as it orbits within aluminum-alloy vacuum chambers running through the centers of the electromagnets.⁵¹

There are 40 straight sections, or sectors, in the storage ring of this 3rd generation synchrotron. Five sectors are used for beam injection and radio frequency equipment. The remaining 35 are equipped with insertion devices. Each sector may have at least 2 beamlines which extend up to 75 meters from ring across the experimental hall floor. One of the beamlines begins at a bending magnet. The other beamline begins at an insertion device (undulator or wiggler).

The work described in the experimental part of this thesis was carried out at sector 16, the High-pressure Collaborative Access Team (HPCAT). HPCAT is a sector dedicated to high-pressure research and it has two BM (BMB, BMD) and two ID operational beamlines (IDB, IDD). The ID beamline is being extended to a third ID hutch (ID-E) for selected experiments. The maintenance and operations costs for an 8-hour shift at a beamline amount to ~\$1K. The annual budget of the APS is of about \$2 billion. That is why experimental time (or beamtime) is very valuable and experiments need to

be carefully designed to make the most of the allotted time. Hence the time variable has a crucial influence in the already challenging aspects of a high-pressure experiment.

CHAPTER 3

EXPERIMENTAL

3.1. Ambient Pressure X-ray Diffraction

Commercially available samples of TiH_2 (Alfa Aesar) of stated purity 99% were used in the studies reported here. Conventional angle dispersive X-ray diffraction patterns were collected in Θ - 2Θ Bragg-Brentano geometry, using a PANalytical X'Pert PRO X-ray diffractometer with $\text{Cu K}\alpha$ radiation (1.54056 \AA , 40 kV, 40 mA) and an X'Celerator solid state detector. The sample was placed in a TTK 450-Low-Temperature Chamber from Anton Paar, especially designed for variable-temperature X-ray diffraction studies. The patterns were recorded with step size of $0.008^\circ 2\Theta$ in the range 30° to $80^\circ 2\Theta$ and 24 s per step. The temperature was varied from 0°C up to 120°C in steps from 3° to 20°C in two series. In the first series temperature was gradually decrease dfrom 25°C down to 0°C . In the second series a new sample of TiH_2 was heated from 25°C up to 120°C .

3.2. High-Pressure Synchrotron X-Ray Diffraction

Every setup for high-pressure powder X-ray diffraction consists of a synchrotron storage ring, X-ray optics including filtering monochromation, collimating, condensating, the high-pressure vessel (ex. DAC), detector and data-analysis software. This can be

supplemented by a cryostat for very low-temperature studies or laser or resistive heating for high-temperature studies.⁴⁰ High-pressure investigations of materials are usually carried out on polycrystalline powders because single crystals do not usually survive the abrupt volume changes which occur at discontinuous phase transitions.³⁹ A complete experiment includes a compression cycle and a subsequent decompression cycle, however in practice the decompression cycle is often left out because of beamtime limitations or worse, because of anvil failure.⁴⁰

3.2.1. Energy-Dispersive X-Ray Diffraction (EDXRD)

In a first series of experiments the structural stability of TiH_2 under compression was investigated up to 34 GPa at ambient temperature.⁵² For *in situ* energy-dispersive, high-pressure X-ray diffraction studies, the powdered sample was compressed in a Livermore Mao-Bell-type diamond anvil cell (DAC). A rhenium gasket was preindented to a thickness of 70 μm , using diamonds with 420 μm diameter culets. The sample chamber consisted of a 130 μm diameter hole, drilled in the preindented rhenium gasket. Sample loading was done in air atmosphere. A few grains of ruby powder were included and used to measure the pressure using the pressure scale of Mao.⁵³ No pressure-transmitting medium was used in this experiment. The time gap between a pressure raise and the subsequent X-ray measurement was about 10 min in order to allow the pressure inside the sample chamber to equilibrate.

All energy-dispersive X-ray diffraction patterns were collected at beamline 16BMD of the High-pressure Collaborative Access Team (HPCAT), Advanced Photon Source (APS), Argonne National Laboratory, Chicago. The energy range of the white

beam spectrum accessible at beamline 16BMD was 5 to 75 keV. The beam was focused to a 10x10 μm spot using 200 mm long KB-mirrors attuned to one milliradian and a 30 μm diameter Mo cleanup pinhole was used to eliminate beam tails. The diffracted x-rays were analyzed with a liquid nitrogen-cooled germanium solid-state point detector placed at a 2θ angle of $12.007(9)^\circ$. The energy spectrum of the germanium-detector was calibrated with radioactive check source of ^{109}Cd using Ag K_α , $K_{\beta 1}$, $K_{\beta 2}$ and Ag $_{\gamma 1}$ decay radiation. The diffraction angle was confirmed by measuring the pattern of a CeO_2 standard from NIST. The intensities of the patterns was subsequently scaled according with the energy-dependent intensity of the incident beam.

The diffraction patterns collected with both the conventional as well as the synchrotron X-ray diffraction techniques were analyzed with software such as Powder Cell⁵⁴ and Topas 2.1 Bruker AXS⁵⁵ was used to perform Rietveld full-profile structural refinements.

3.2.2. Angle-Dispersive X-Ray Diffraction (ADXRD)

In a second series of experiments high-resolution, angle-dispersive, synchrotron X-ray diffraction (ADXRD) experiments were carried out. The structural stability of TiH_2 was investigated in two separate compression runs, first up to 21 GPa and then up to 90 GPa and in subsequent decompression to ambient conditions. ADXRD measurements were performed at the 16-IDB beamline (Figure 8) of the High Pressure Collaborative Access Team (HPCAT) of the Advanced Photon Source, Argonne National Laboratory.

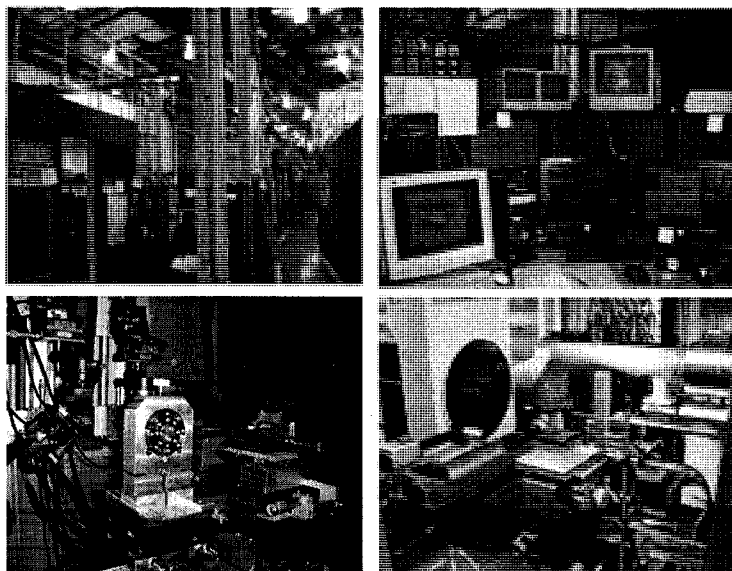


Figure 8. Pictures of the HPCAT at APS. Clockwise from top left: experimental hall, control area, DAC placed inside the ID-B hutch, image plate and CCD detectors.

A $320 \times 300 \mu\text{m}^2$ monochromatic x-ray beam with a wavelength $\lambda = 0.3682 \text{ \AA}$, $\lambda = 0.4136 \text{ \AA}$, $\lambda = 0.3931 \text{ \AA}$ (depending on the time of the experimental run) was focused down to a $\sim 6 \times 6 \mu\text{m}$ spot using Kirkpatrick-Baez (KB) 200 mm mirrors. Diffraction images were recorded with a MAR345 imaging plate as a detector and were integrated and corrected for distortion using the FIT2D⁵⁶ software. The acquisition time was 60s, 30s, or 20s. The sample-detector distance ($\sim 350 \text{ mm}$) and geometric parameters were calibrated at the beginning of each run using a CeO_2 standard from NIST. Samples of TiH_2 powder (Alfa Aesar) of stated purity 99% were used in the studies reported here. The sample was compressed in a symmetric diamond anvil cell (DAC) (Figure 9). A rhenium gasket was preindented to a thickness of $\sim 50 \mu\text{m}$, using diamonds with $320 \mu\text{m}$ diameter culets. The

sample chamber consisted of a 90 μm diameter hole, drilled in the preindented rhenium gasket. Sample loading was done in air atmosphere.

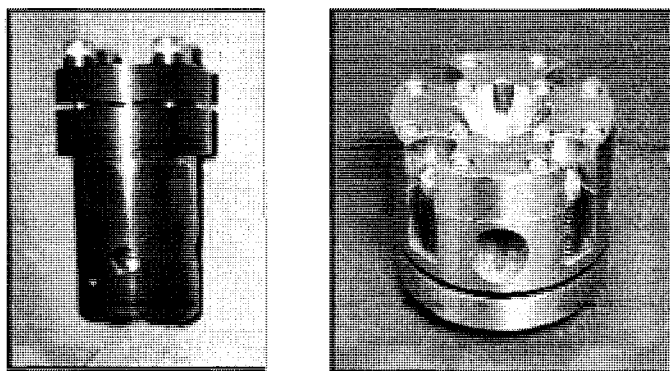


Figure 9. Diamond anvil cells used in the high-pressure experiments. Left: Livermore Mao-Bell type DAC used in the collection of EDXRD patterns of TiH_2 ; right: symmetric Japanese design symmetric DAC from Syntec used in the collection of ADXRD patterns of TiH_2 .

A few ruby microspheres were placed in the sample chamber and used to measure pressure using the pressure scale of Mao.^{48, 57} A few grains of gold were also included and used to measure pressure using the equation of state of Anderson et al.⁵⁸ The first compression sequence was carried up to 21 GPa with an ethanol-methanol mixture (4:1 by vol.) which served as a quasi-hydrostatic pressure-transmitting medium. The second compression run was carried out up to ~ 90 GPa on neat TiH_2 (without a pressure medium). The time gap between a pressure increase and the subsequent X-ray measurement was about 10 min in order to allow the pressure inside the sample

chamber to equilibrate. The diffraction patterns were indexed with Powder Cell⁵⁴ and Topas 2.1⁵⁹ was used to perform Rietveld full-profile structural refinements.

CHAPTER 4

RESULTS

4.1. On the structure of TiH_2

Figure 10 illustrates models of the crystal structures of TiH_2 . Metal hydrides from the IVB group form a cubic phase which can be non-stoichiometric over a wide range as well as a tetragonal phase, which is usually deficient in hydrogen.¹⁰

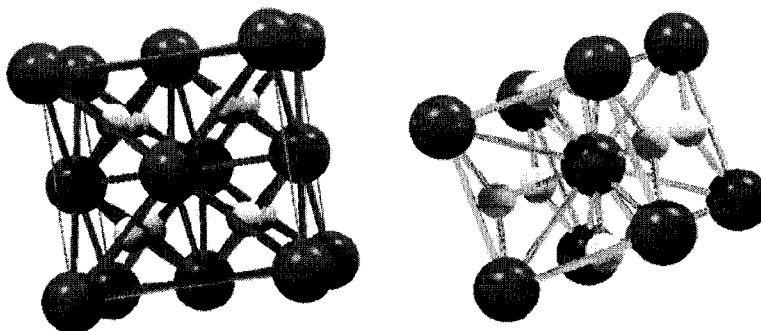


Figure 10. Models of the cubic $Fm\bar{3}m$ (left) and the tetragonal $I4/mmm$ (right) crystal lattices of TiH_2 . Pink and white spheres represent titanium and hydrogen atoms, respectively. The tetragonal structure is found to appear at low temperatures and high-pressures.

For titanium hydride in particular the room temperature form (25°C) is cubic while the tetragonal form has only been detected at near-stoichiometric compositions

and slightly below room temperature. Like for many other dihydrides of transition metals, the cubic phase of TiH_2 has a fluorite-type structure (CaF_2) where Ti atoms form an *fcc* lattice and the hydrogen atoms are situated at the tetrahedral interstitial positions of the metal lattice. The tetragonal phase of TiH_2 has a distorted fluorite structure (Fig. 10) where one crystallographic axis is shortened and two other are lengthened.⁶⁰ In the metallic matrix of TiH_2 (cubic or tetragonal) there are two tetrahedral interstitial sites per atom Ti occupied by hydrogen.¹³ There is also one empty octahedral interstitial site per atom Ti which has been experimentally shown to be empty.¹³

Table 1 Summary of the various experimental techniques and experimental runs carried out on TiH_2 .

Type of Experiment	Radiation	Pressure Range	Pressure Medium	Temperature
conventional XRD	CuK_α	atm.	---	$0 \rightarrow 25^\circ\text{C}$
conventional XRD	CuK_α	atm.	---	$25 \rightarrow 120^\circ\text{C}$
EDXRD	synchrotron	$0 \rightarrow 34 \text{ GPa}$	neat sample	25°C
EDXRD	synchrotron	$34 \rightarrow 0 \text{ GPa}$	neat sample	25°C
ADXRD	synchrotron	atm.	---	25°C
ADXRD	synchrotron	$0.6 \rightarrow 21 \text{ GPa}$	methanol-ethanol	25°C
ADXRD	synchrotron	$21 \rightarrow 0 \text{ GPa}$	methanol-ethanol	25°C
ADXRD	synchrotron	$0 \rightarrow 90 \text{ GPa}$	neat sample	25°C
ADXRD	synchrotron	$90 \rightarrow 0 \text{ GPa}$	neat sample	25°C

In the next section results of the multi-technique investigations into the structural properties of TiH_2 are presented in the following order: first conventional X-ray diffraction at ambient pressure combined with moderately high temperatures; next energy-dispersive synchrotron X-ray diffraction up to 34 GPa; finally high resolution angle-dispersive synchrotron X-ray diffraction up to almost a mega bar pressure, 90 GPa. Table 1 summarizes the experimental techniques and the conditions of the various runs.

4.2. Ambient Pressure, High-Temperature X-ray Diffraction

Temperature-dependent conventional X-ray diffraction patterns were collected from 25°C down to 0°C as well as from 25°C up to 120°C in variable steps (from 4 to 20°C). The smallest temperature step was chosen taking into consideration the limits of the accuracy of the temperature stage, which is about 3°C. Figure 11 shows the complete set of X-ray diffraction patterns collected in two experimental runs. The diffraction lines observed in all patterns correspond to TiH_2 . At 20°C and above, TiH_2 has a cubic structure and belongs to space group Fm-3m (225).^{26, 61} A Rietveld full-profile structural refinement shown in Figure 12 demonstrates an excellent match between the observed and the calculated x-ray pattern. The refined unit cell parameter of the cubic phase is $a=4.4492(28)$ Å and the refined volume and X-ray density are $V=88.07(17)$ Å³ and $d=3.7630(72)$ g/cm³, respectively (Fig 12).

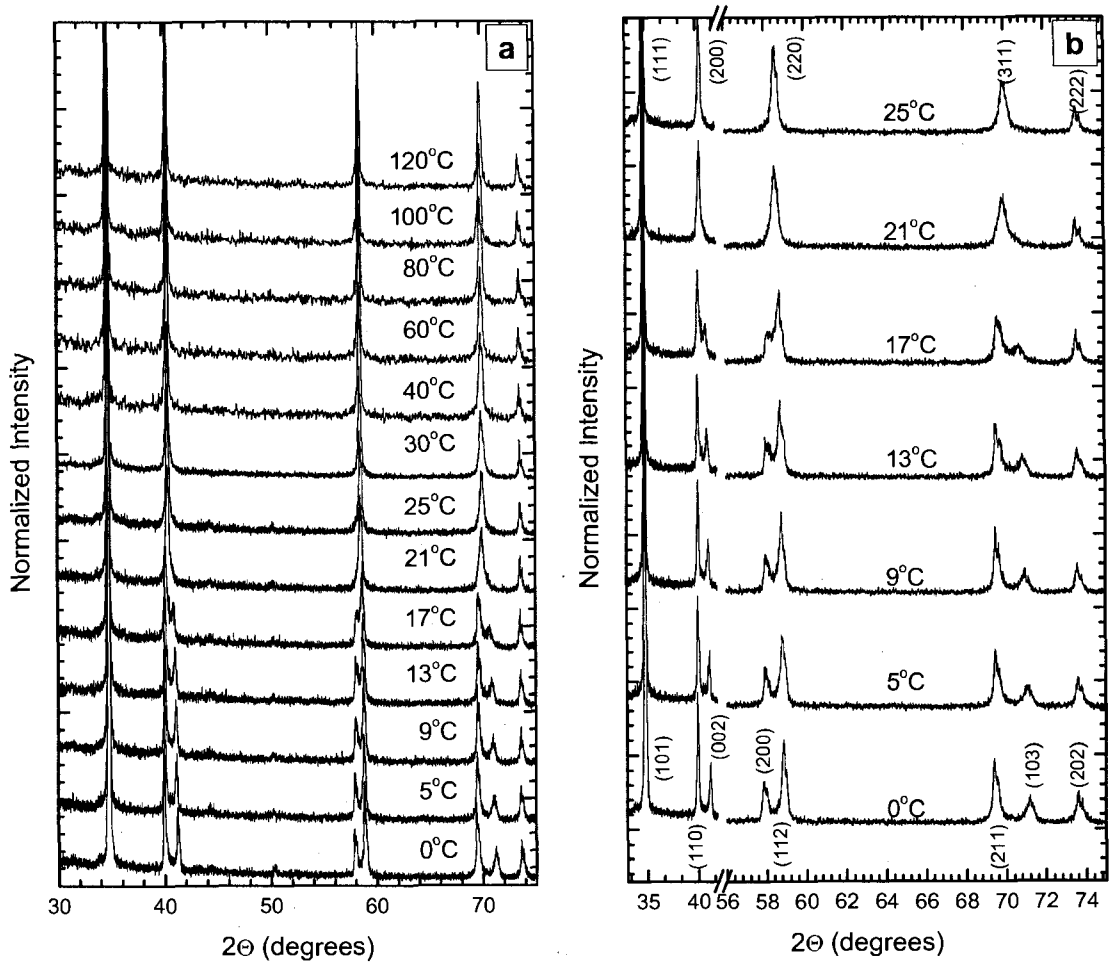


Figure 11. Conventional angle dispersive X-ray diffraction patterns of TiH_2 collected as a function of temperature between 0 and 120°C (a); and (b) zoom showing line splitting between 25°C and 0°C, which evidence the phase transition from the cubic to the tetragonal structure. Individual reflections are identified with Miller indices for the cubic structure (0°C plot) and for the tetragonal structure (25°C plot).

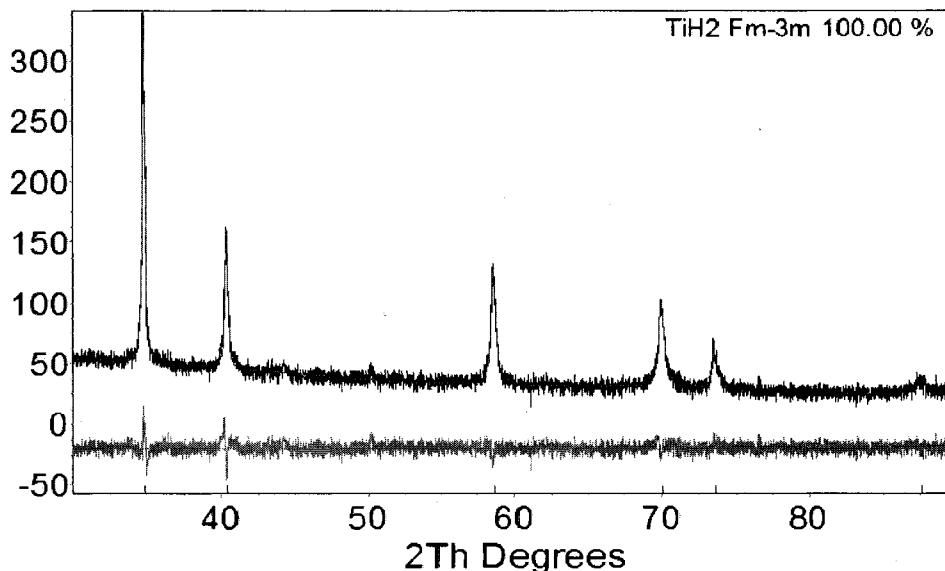


Figure 12. Rietveld full-profile structural refinement of the conventional angle-dispersive x-ray diffraction pattern of TiH_2 collected at 25°C . The refinement was carried out using the cubic space group Fm-3m (225). The blue and red lines represent experimental and modeled patterns, respectively. The grey line at the bottom represents the difference between the observed and the refined profile.

Below 20°C three diffraction lines of the cubic phase (200), (220) and (311) start showing some profile asymmetry (Figure 11). At about 17°C each line splits into two new diffraction lines and cubic TiH_2 undergoes a phase transition to a lower symmetry, tetragonal structure. This structural change is attributed to a Jahn-Teller γ - γ' phase transition of the second kind, resulting in a tetragonal structure.¹³ Specifically the (200) cubic line splits into the tetragonal (110) and (002), the cubic (220) line splits into tetragonal (200) and (112) and the (311) cubic line splits into tetragonal (211) and (103) lines.

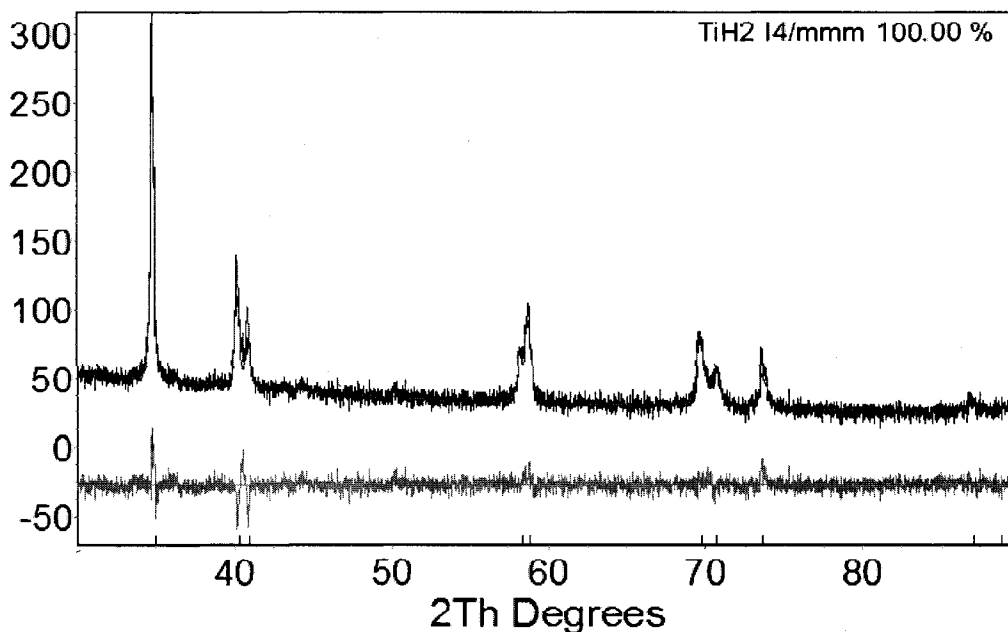


Figure 13. Rietveld full-profile structural refinement of the conventional ADXRD pattern of TiH_2 collected at 17°C , which is the temperature at which the cubic to tetragonal phase transition occurs. The refinement was carried out using the group $I4/mmm$ (139). The blue and red lines represent experimental and modeled patterns, respectively. The grey line at the bottom represents the difference between the observed and the refined profile.

The tetragonal structure is preserved down to 0°C . The new structure belongs to the space group $I4/mmm$ (139).¹³ A Rietveld full-profile structural refinement of the pattern collected at 17°C , shown in Figure 13, is in excellent agreement with the observed x-ray pattern. The refined unit cell parameters of the tetragonal phase are $a=3.1635(26)\text{ \AA}$, $c=4.4023(37)\text{ \AA}$ with a volume and density of $V=44.056(8)\text{ \AA}^3$ and

$d=3.7613(7) \text{ g/cm}^3$ respectively. When the sample is heated back up to 20°C , it reverts to the original cubic structure.

It is known that group IVB metals form stable dihydrides (ex. TiH_x) over a wide range of concentrations, where they assume the CaF_2 -type structure (*fcc*). The tetragonal distortion of the lattice, which is observed for the group IVB hydrides (when the concentration of H approaches $x=2$) below a critical temperature can be attributed to a Jahn-Teller effect, as was shown in theoretical studies.¹² As shown in this and other works the distortion of the cubic lattice occurs for TiH_2 at 17°C . The Fermi level of group IVB metal cubic dihydrides falls in a peak of the density of states (DOS). The maximum DOS value arises from a flat branch of degenerate metal *d*-states in the Γ -L direction of the *fcc* Brillouin zone. The quadratic distortion lifts this degeneracy and leads to a lowering of the Fermi level and of the DOS at E_F .¹² The face centered cubic to face centered tetragonal distortion also lowers the DOS at E_F .¹²

4.3. Energy-Dispersive Synchrotron X-Ray Diffraction (EDXRD) of TiH_2 up to 34 GPa

Energy-dispersive, synchrotron X-ray diffraction (EDXRD) patterns of TiH_2 were collected in the diamond anvil cell (DAC), during compression from ambient pressure up to 34 GPa, and on successive decompression back to ambient conditions. Figure 14 shows the sequence of diffraction patterns acquired *in situ* in compression, at ambient temperature. All the diffraction lines present belong to TiH_2 . In the first pattern, collected in the DAC at ambient pressure, the identified crystal structure is cubic. As pressure is increased, all diffraction lines shift towards higher energies or lower *d*-

spacings, and new lines appear as a result of splitting. Upon compression to 2.2 GPa, TiH_2 undergoes a phase transition to a lower symmetry structure, characterized by a tetragonal distortion of the unit cell (Fig. 14). The observed changes in the high-pressure patterns indicate that the tetragonal phase of TiH_2 gradually densifies with pressure and compresses smoothly up the highest investigated pressure, 34 GPa (Fig. 14). After decompression to ambient conditions, the tetragonal TiH_2 reverts back to its initial cubic structure. Because no pressure-transmitting medium was used, the diffraction lines are broadened due to non-hydrostatic stresses. In addition some Bragg lines' intensities vary between patterns because of the large grain size of the sample, which resulted in a reduction of counting statistics (Fig. 14). In conclusion, we observe that above 2 GPa the cubic lattice undergoes a pressure-induced phase transformation into a lower symmetry structure, which remains stable to 34 GPa. The 2 GPa transition pressure is most probably an upper bound. The new tetragonal phase is a distorted fluorite structure with one crystallographic axis shortened and the two others lengthened. In this structure the H atoms are still situated in tetrahedral interstitial positions within the basic crystal lattice (Fig. 10).

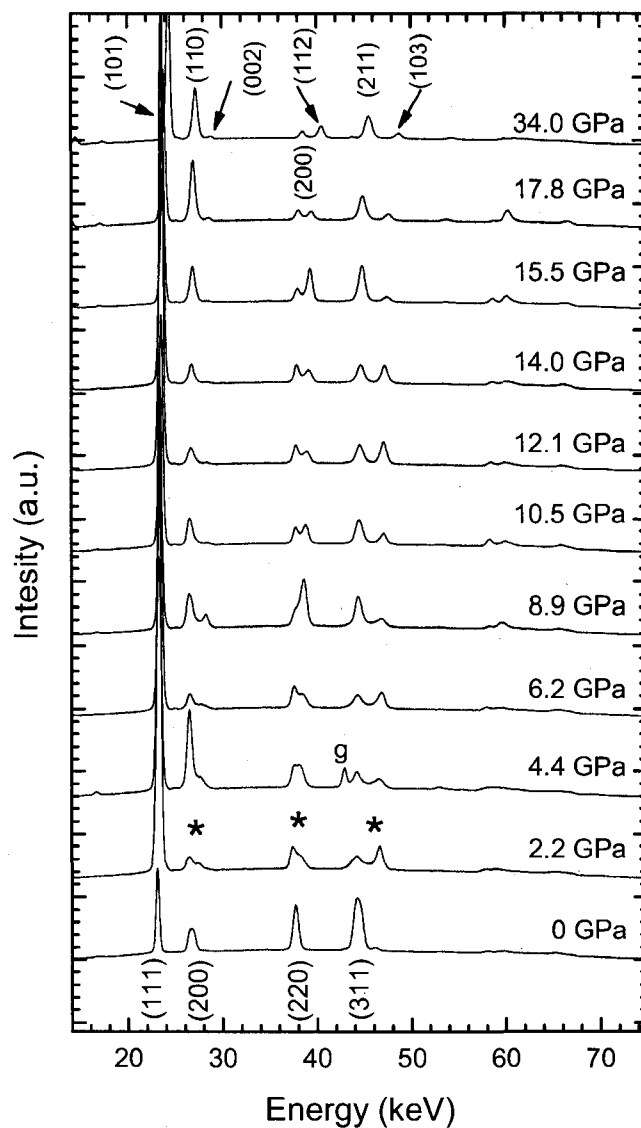


Figure 14. Energy-dispersive, synchrotron X-ray diffraction patterns collected in the diamond anvil cell, during compression from ambient pressure up to 34 GPa: all patterns were corrected for the energy-dependent intensity profile of the incident x-ray beam before structural refinements were carried out. Individual reflections are identified with Miller indices for the cubic structure (0 GPa plot) and for the tetragonal structure (34 GPa plot). Stars mark the appearance of new lines that indicate the phase transition.

4.4. Angle-Dispersive Synchrotron X-Ray Diffraction (ADXRD) of TiH_2 up to 90 GPa

In order to compare conventional and synchrotron X-ray diffraction of TiH_2 an ADXRD pattern was collected at ambient pressure, outside the DAC. A Rietveld full-profile structural refinement of the ADXRD pattern is shown in (Figure 15). The mismatch in intensities is attributed to the large grain size of the sample and the very small x-ray beam size. Both of these factors contribute to reduce the image plate statistics. In this respect the synchrotron ADXRD pattern collected (Fig. 15) is not as representative of the structure of TiH_2 as the conventional pattern.

High-pressure ADXRD experiments were performed in two separate runs. In the first experimental run, high pressure patterns of TiH_2 were collected in the DAC, on compression from 0.6 GPa up to 21 GPa using a methanol-ethanol mixture as a quasi-hydrostatic pressure transmitting medium. Figure 16 illustrates selected x-ray diffraction patterns of this run together with the ambient pressure pattern collected outside the DAC. Diffraction lines of TiH_2 are indexed by the corresponding Miller indices. In the first pattern, collected at ambient pressure (Fig. 15) the crystal structure identified from the refinement is cubic. As pressure is increased to 0.6 GPa new reflections appear as a result of splitting. TiH_2 transitions to a lower symmetry structure, which is characterized by a tetragonal distortion of the unit cell (Fig 16). More precisely, as can be seen in Figure 16 the cubic line (200) splits into the tetragonal lines (110) and (002), the cubic line (220) splits into the tetragonal lines (200) and (112), the cubic line (311) splits into the tetragonal lines (211) and (103), and the cubic line (331) splits into the tetragonal lines (301) and (213). As pressure is increased beyond 0.6 GPa all the diffraction lines

shift towards higher 2θ angles or lower d -spacings. The observed modifications of the high-pressure patterns imply that the tetragonal phase of TiH_2 gradually densifies, compressing smoothly up to 21 GPa. Decompression from 21 GPa to ambient pressure showed that the phase transition is reversible.

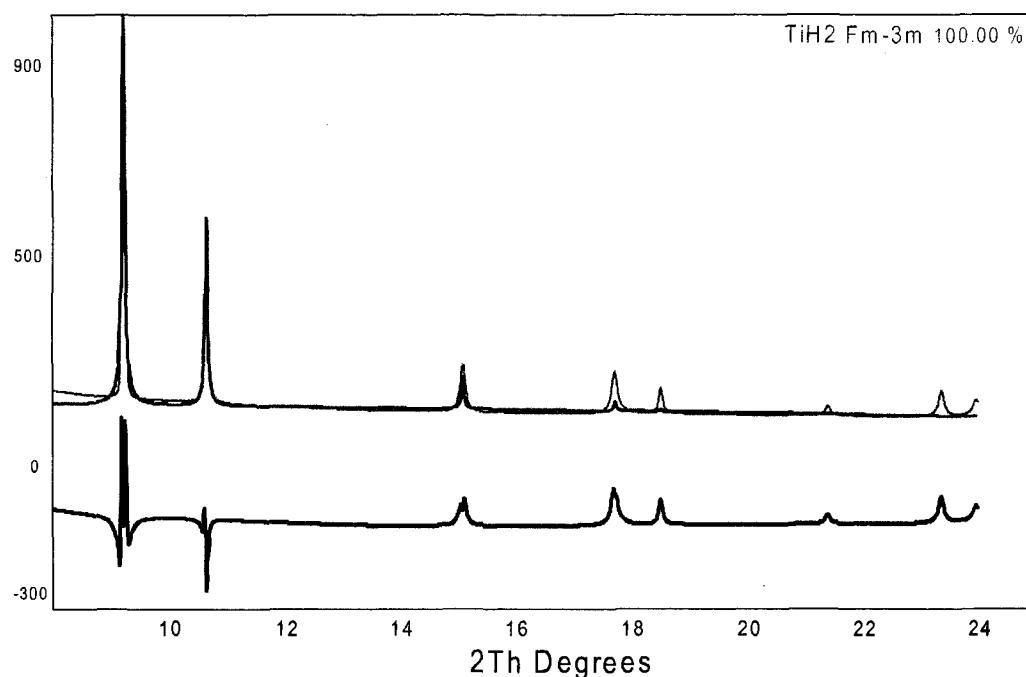


Figure 15. Rietveld full-profile structural refinement of the synchrotron ADXRD pattern of TiH_2 collected with the synchrotron beam, outside the DAC. The refinement was carried out using the cubic space group Fm-3m (225). The blue and red lines represent experimental and modeled patterns, respectively. The grey line at the bottom represents the difference between the observed and the calculated peak profiles.

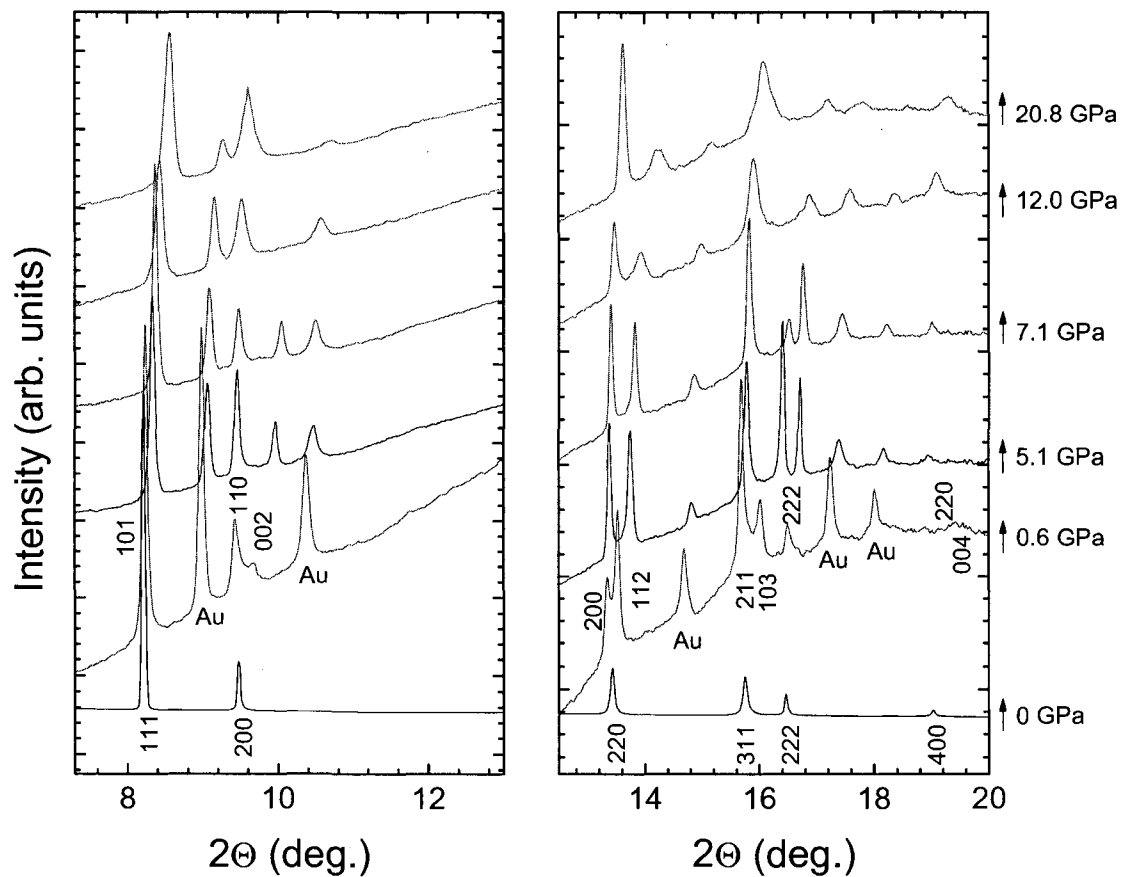


Figure 16. In situ, synchrotron ADXRD patterns collected in the DAC, during compression from ambient pressure up to 21 GPa: Individual reflections are identified with Miller indices for the cubic structure on the 0 GPa plot and for the tetragonal structure on the 0.6 GPa plot. Lines due to the gold pressure marker are indicated with Au. The ambient (0 GPa) pressure pattern was collected outside the DAC and does not display the diffuse diamond background.

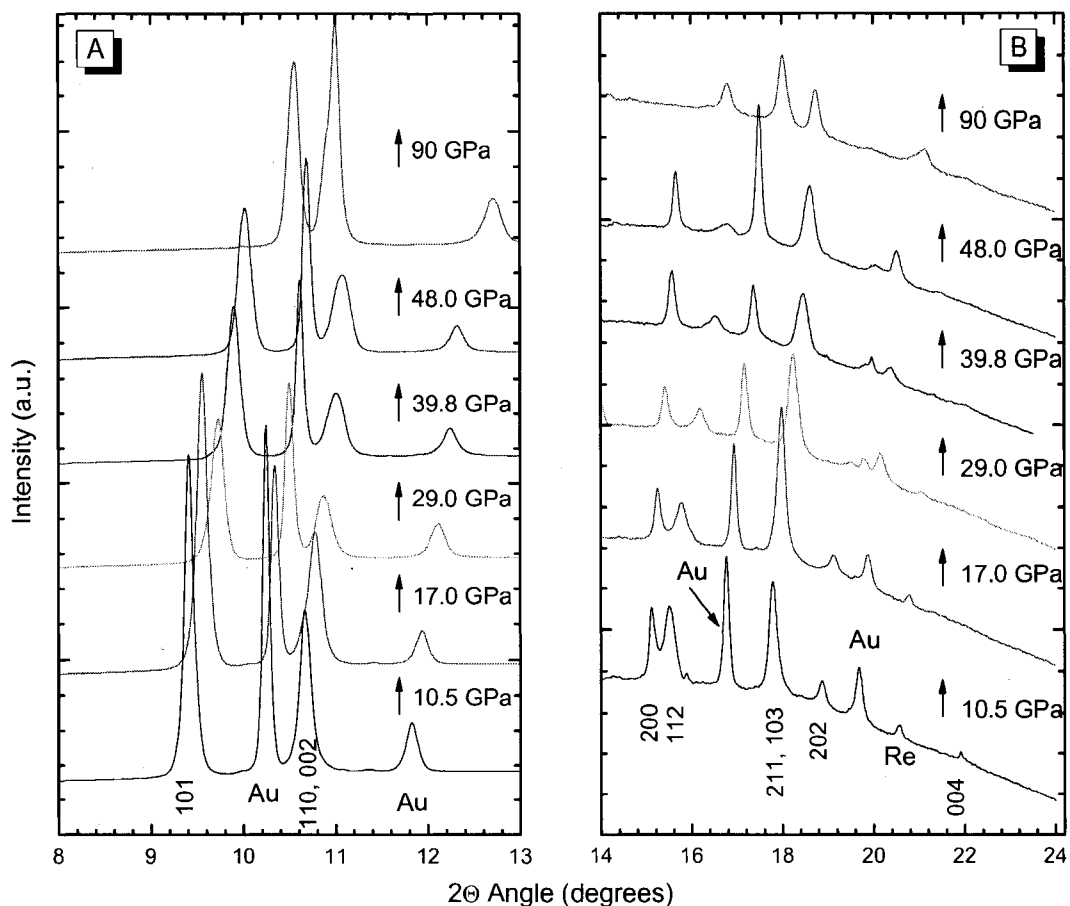


Figure 17. In situ, synchrotron ADXRD patterns collected in the DAC, during compression from ambient pressure up to 90 GPa. Individual reflections are identified with Miller indices for the tetragonal structure of TiH_2 (10.5 GPa plot). Lines due to the gold pressure marker are indicated with Au. The higher 2θ range is displayed on a different intensity scale in order to magnify the details of the pattern.

In a second series of high-pressure synchrotron ADXRD experiments TiH_2 was studied on compression from ambient pressure up to 90 GPa. Selected diffraction patterns are shown in Figure 17. Miller indices indicate reflections belonging to the

tetragonal structure of TiH₂. Since no pressure-transmitting medium was used in this experimental run, the diffraction lines are broadened significantly due to non-hydrostatic stresses. As shown in Figure 17, TiH₂ compresses smoothly up to the highest pressure investigated, without any further phase transitions. At 90 GPa the (111) reflection of gold as well as the (110) reflection of TiH₂ are overlapped. After decompression from 90 GPa to ambient conditions the high-pressure tetragonal structure of TiH₂ was found to persist what contrasts with what was found on decompression from the first ADXRD experiment – 21 GPa – as well as from the EDXRD decompression down from 34 GPa.

The intensity of diffraction lines is proportional to the square of the wave amplitude or of the structure factor:

$$I_{hkl} \propto F_{hkl}^* F_{hkl} = f_1^2 + f_2^2 + 2f_1f_2\cos(\phi_{hkl})$$

Analyzing the above formula, depending on the phase difference, which is a function of atom positions and of (hkl), the cosine term will either augment or diminish the actual intensity of a reflection. This variation adds to the fact that the scattering factor diminishes with increasing angle and yields an overall decrease in the observed intensities of reflections with increasing angle (with some discontinuities for positive cosine values).

A feature proper to X-ray diffraction patterns collected with the sample placed in a DAC is that the inelastic scattering events occurring in the diamond add an undesirable diffuse background. This feature can be seen on any cascade plot of XRD patterns collected under pressure. This background can affect the measured intensities of

reflections and cause a mismatch between measured and calculated intensities in a structural refinement.

CHAPTER 5

DISCUSSION AND CONCLUSIONS

Selected results of experimental studies outlined in the previous chapter are further discussed in this chapter. First, we begin by looking into the issues of establishing equations of state for condensed matter at extreme pressures. Next an equation of state is determined for TiH_2 for both the EDXRD results as well as for the ADXRD results. In what follows, the discussion is extended to the type of pressure-induced phase transition as well as the various issues associated with achieving extreme pressure (DAC preparation, preferred orientation, hydrostaticity...). Finally conclusions of the multi-technique investigations are presented.

5.1. Equation of State of Titanium Hydride

5.1.1. Equations of State for Solids at Extremely High-pressures

An equation of state (EoS) is a relation describing, for a given material, the connection between pressure (P), volume (V) and temperature (T). This work treats of a solid and for solids the temperature has a much smaller influence on the P-V relationship. Temperature can then be either omitted or factored in as a small correction term to an isothermal equation of state. Moreover, for a solid we can use the

zero temperature equation of state and account for the effect of temperature by using thermal expansion coefficients.

Bulk modulus (K) or constant incompressibility, measures a substance's response (strain) to a uniform compression (stress) and is defined:

$$K = - \frac{\text{change in pressure}}{\text{fractional change in volume}} = - \frac{\partial P}{\frac{\partial V}{V}} = -V \frac{\partial P}{\partial V}$$

Or in terms of density ρ the bulk modulus is:

$$K = \rho \frac{\partial P}{\partial \rho}$$

At low pressures, specifying the value of K (at constant temperature) is an isothermal equation of state and is applicable to solids and liquids. This is a description of deformation which is exceedingly small relative to the size of the material and it called an infinitesimal strain theory for hydrostatic compression. The bulk modulus was assumed constant (K_o). However if we integrate the above definition to obtain density we get:

$$\frac{\partial \rho}{\rho} = \frac{1}{K_o} \partial P$$

$$\int_{\rho_o}^{\rho} \frac{\partial \rho'}{\rho'} = \int_0^P \frac{1}{K_o} \partial P' \rightarrow \ln \left(\frac{\rho}{\rho_o} \right) = \frac{P}{K_o} \rightarrow \rho = \rho_o e^{P/K_o}$$

This shows that of the above equation of state to hold the pressure must be very small (so that K_o can remain constant).⁶² In fact as P increases, then ρ would increase exponentially. However experimental observations on materials subjected to pressures found in the Earth show that the increase in density becomes more difficult as pressure is raised. That is why the above EoS is an infinitesimal strain theory.

Murnaghan proposed the simplest relationship that accounts for density increasing more slowly as pressure is raised, and this is known as the Murnaghan equation of state (“integrated linear theory”⁶³):

$$K = K_o + K'_o P$$

with $K' = K'_o = \left(\frac{\partial K}{\partial P}\right)_{P=0}$ (independent of pressure)

and inserting the definition of K from above:

$$K_o + K'_o P = \rho \frac{\partial P}{\partial \rho}$$

$$\int_{\rho_o}^{\rho} \frac{d\rho'}{\rho'} = \frac{1}{K_o} \int_0^P \frac{dP'}{\left(1 + \frac{K'_o P'}{K_o}\right)} = \frac{1}{K_o} \frac{K_o}{K'_o} \int_1^{1 + \frac{K'_o P}{K_o}} \frac{dy}{y} = \frac{1}{K'_o} [\ln(y)]_1^{1 + \frac{K'_o P}{K_o}} \text{ where } y = 1 + \frac{K'_o P'}{K_o}$$

$$\ln\left(\frac{\rho}{\rho_o}\right) = \ln\left(1 + \frac{K'_o}{K_o} P\right)^{\frac{1}{K'_o}}$$

$$\frac{\rho}{\rho_o} = \left(1 + \frac{K'_o}{K_o} P\right)^{\frac{1}{K'_o}}$$

Finally, the above equation can be inverted to obtain an expression for the Murnaghan EoS (“integrated linear theory”) in P as a function of V :

$$P = \frac{K_o}{K'_o} \left[\left(\frac{\rho}{\rho_o}\right)^{K'_o} - 1 \right] = \frac{K_o}{K'_o} \left[\left(\frac{V}{V_o}\right)^{-K'_o} - 1 \right]$$

The Murnaghan equation is reasonable for many materials as long as $0 < P < K_o/2$.

The finite strain calculations have been further developed in order to cover a wider range of pressure. Nowadays, the most widely used formalism is the so called Birch-Murnaghan equation of state. It is founded on the theoretical treatment of finite strains carried out by A. Love,⁶⁴ further modified by Murnaghan and adapted to

geosciences by Birch. According to Love's definition of strain, in a strained body the change in length in any line is invariant with respect to the choice of axes or to rotations.

Let's assume that a solid is undergoing hydrostatic compression. As a result of the stress, two points in the material separated by a distance D in direction x , are now separated by a smaller distance D' also in the x -direction ⁶⁵:

$$\frac{D'}{D} = \frac{\partial(x+u)}{\partial x} = 1 + \frac{\partial u}{\partial x}$$

where u is the displacement of any point, and it's derivative has a negative sign since for compression $D'/D < 0$. So if there is no displacement then $D'=D$.

Strain ϵ , is defined from the square of the quotient of distances and the square in the following definition is used so that the square of displacement will give a symmetrical expression when three, in lieu of one, components are considered ⁶⁴:

$$\left(\frac{D'}{D}\right)^2 = \left(1 + \frac{\partial u}{\partial x}\right)^2 = 1 + 2\frac{\partial u}{\partial x} + \frac{\partial^2 u}{\partial x^2} = 1 + 2\left[\frac{\partial u}{\partial x} + \frac{1}{2}\left(\frac{\partial u}{\partial x}\right)^2\right] = 1 + 2\epsilon$$

As a consequence, the volume of the strained and unstrained states is expressed as a function of ϵ :

$$\frac{V}{V_o} = \left(\frac{D'}{D}\right)^3 = (1 + 2\epsilon)^{\frac{3}{2}}$$

When a material is compressed the strain is positive, so it is then suitable to redefine strain as:

$$f = -\epsilon = -\left\{\frac{\partial u}{\partial x} + \frac{1}{2}\left(\frac{\partial u}{\partial x}\right)^2\right\}$$

As a consequence the expression for volume becomes:

$$\frac{V}{V_o} = (1 - 2f)^{\frac{3}{2}}$$

We can write now a definition of strain f in terms of V :

$$f = \frac{1 - \left(\frac{V}{V_o}\right)^{\frac{2}{3}}}{2}$$

Again, since mass is constant we can eliminate it so that we obtain a definition of strain f in terms of density:

$$f = \frac{1 - \left(\frac{\rho}{\rho_o}\right)^{\frac{2}{3}}}{2}$$

This formulation is of interest if the Helmholtz free energy F ($F=U-TS$), is a strongly convergent polynomial function of f , written as:

$$F = A_2 f^2 + A_3 f^3 + A_4 f^4 + A_5 f^5 + \dots$$

Then we know from thermodynamics that:

$$P = -\frac{\partial F}{\partial V}|_T; \quad K = V \frac{\partial P}{\partial V}|_T; \quad K' = \frac{\partial K}{\partial P}|_T; \quad K'' = \frac{\partial^2 K}{\partial P^2}|_T.$$

In order to find an expression for P as a function of volume we need the derivative:

$$\frac{df}{dV} = \frac{1}{2} \left(-\frac{2}{3}\right) \left(\frac{V}{V_o}\right)^{-\frac{1}{3}} \frac{1}{V_o} = -\frac{1}{3V_o} \left(\frac{V}{V_o}\right)^{-\frac{1}{3}} = -\frac{1}{3V_o} (1 - 2f)^{-\frac{1}{2}}$$

Next we have:

$$P = -\frac{\partial F}{\partial V} = -\frac{dF}{df} \frac{df}{dV} = -\frac{d(A_2 f^2 + A_3 f^3 + A_4 f^4 + A_5 f^5 + \dots)}{df} \frac{df}{dV}$$

$$P = -(2A_2 f^1 + 3A_3 f^2 + 4A_4 f^3 + \dots) \left[-\frac{1}{3V_o} (1 - 2f)^{-\frac{1}{2}} \right]$$

$$P = \frac{1}{3V_o} \left(2A_2 f^1 - 4A_2 f^{\frac{1}{2}} + 3A_3 f^2 - 6A_3 f^{\frac{3}{2}} + 4A_4 f^3 - 8A_4 f^{\frac{5}{2}} + \dots \right)$$

By substituting the conditions $P=0$, $K=K_o$, $K'=K_o'$, $K''=K_o''$ at $f=0$ one can eliminate the coefficients A and thus represent P , K , K' and K'' in terms of K_o , K_o' , K_o'' .

Finally, we obtain the Love-Murnaghan formalism for hydrostatic compression with strain defined relative to the unstrained state (or Lagrangian strain):

$$P = \frac{3}{2} K_o \left(\frac{V}{V_o} \right)^{-\frac{1}{3}} \left[1 - \left(\frac{V}{V_o} \right)^{\frac{2}{3}} \right] \left\{ 1 + \frac{3}{4} K_o' \left[1 - \left(\frac{V}{V_o} \right)^{\frac{2}{3}} \right] + \frac{3}{8} \left(K_o K_o'' + K_o' + K_o'^2 - \frac{1}{9} \right) \left[1 - \left(\frac{V}{V_o} \right)^{\frac{2}{3}} \right]^2 + \dots \right\}$$

F. Birch established a formalism based on that of Love and Murnaghan, but using Eulerian strain ϵ^* instead. Eulerian strain is strain relative to the strained state and is expressed by:

$$\left(\frac{D}{D'} \right)^2 = \left(1 - \frac{\partial u}{\partial x} \right)^2 = 1 - 2 \left[\frac{\partial u}{\partial x} - \frac{1}{2} \left(\frac{\partial u}{\partial x} \right)^2 \right] = 1 - 2\epsilon^*$$

$$\epsilon^* = \frac{\partial u}{\partial x} - \frac{1}{2} \left(\frac{\partial u}{\partial x} \right)^2$$

Hence, following the previous reasoning we have:

$$\frac{V_o}{V} = \left(\frac{D}{D'} \right)^3 = (1 - 2\epsilon^*)^{\frac{3}{2}}$$

$$\frac{V}{V_o} = (1 - 2\epsilon^*)^{-\frac{3}{2}} = (1 + 2f^*)^{-\frac{3}{2}}$$

And the Helmholtz free energy as a polynomial series in f^* is:

$$F = B_2 f^{*2} + B_3 f^{*3} + B_4 f^{*4} + B_5 f^{*5} + \dots$$

Continuing the reasoning used in the Love-Murnaghan formalism we differentiate F with respect to V and find the B constants by using the conditions at $f^*=0$. Finally we obtain the Eulerian finite strain equation of state, commonly referred to as the Birch-Murnaghan equation of state:

$$P = \frac{3}{2}K_o \left[\left(\frac{V}{V_o} \right)^{-\frac{7}{3}} - \left(\frac{V}{V_o} \right)^{-\frac{5}{3}} \right] \left\{ 1 + \frac{3}{4}[K'_o - 4] \left[\left(\frac{V}{V_o} \right)^{-\frac{2}{3}} - 1 \right] + \frac{3}{8} \left[K_o K''_o + (K'_o - 4)(K'_o - 3) + \frac{35}{9} \right] \left[\left(\frac{V}{V_o} \right)^{-\frac{2}{3}} - 1 \right]^2 + \dots \right\}$$

The formalism above is most often used with truncation to 2nd order (with K' constrained to 4) or to 3rd order where the equation is reduced to:

$$P = \frac{3}{2}K_o \left[\left(\frac{V}{V_o} \right)^{-\frac{7}{3}} - \left(\frac{V}{V_o} \right)^{-\frac{5}{3}} \right] \left\{ 1 + \frac{3}{4}[K'_o - 4] \left[\left(\frac{V}{V_o} \right)^{-\frac{2}{3}} - 1 \right] \right\}$$

The Birch Murnaghan EoS has been widely used by the scientific community for over 50 years now and it has become synonymous with “finite strain theory”. However in high-pressure physics many researchers have expressed serious reservations⁶⁶⁻⁶⁹ about it. The main reason is that the Love-Murnaghan-Birch approach is empirical and is justified by its mathematical formalism instead of a physical basis, which would be preferable from a physicist’s point of view. The convergence of the polynomial expansion in strain allows to use the Birch-Murnaghan EoS on a set of data but it cannot be extrapolated beyond. Numerous other equations of state (40 at least) have been proposed for use by the high-pressure community (when compression deals with the

GPa range) such as: the Holzapfel EoS,⁷⁰ the natural strain EoS,⁶⁹ the Rydberg-Vinet EoS.^{71, 72} For now however, the use of the Birch-Murnaghan EoS is so widespread that it will probably take a long time for a new, better formalism to supplant it.

5.1.2. Birch-Murnaghan Equation of State of TiH₂ with EDXRD

First, we will analyze the results of energy-dispersive synchrotron X-ray diffraction experiments and next we will focus on the results of high-resolution angle-dispersive synchrotron X-ray diffraction.

Background- and intensity-corrected, high-pressure X-ray diffraction patterns for all the EDXRD measurements shown in Figure 14 could be reasonably well fitted. A Rietveld full-profile structural refinement of the pattern collected in situ, at 2.2 GPa, is shown in Figure 18.

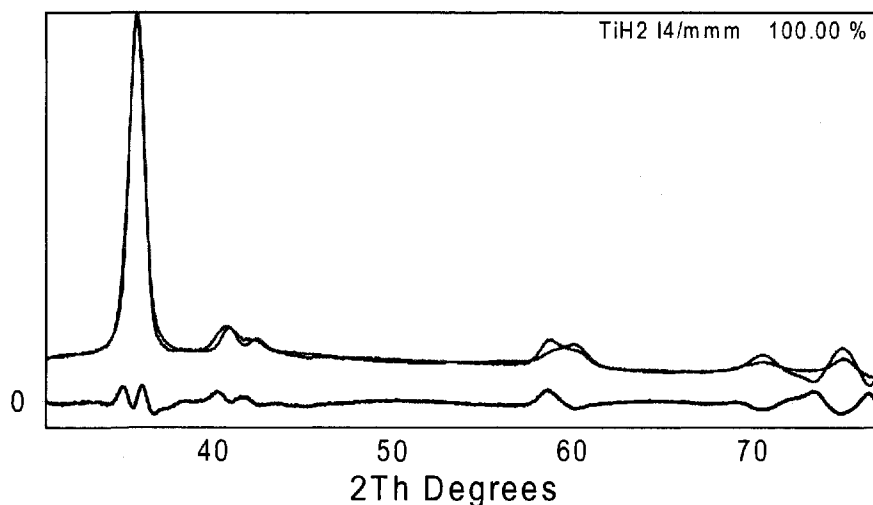


Figure 18. Rietveld full-profile structural refinement of the synchrotron X-ray diffraction pattern of TiH₂ collected at 2.2 GPa and room temperature. The refinement was carried out using the cubic space group I4/mmm (139). The blue and red lines represent experimental and modeled patterns, respectively. The grey line at the bottom represents the difference between the observed and the refined profile.

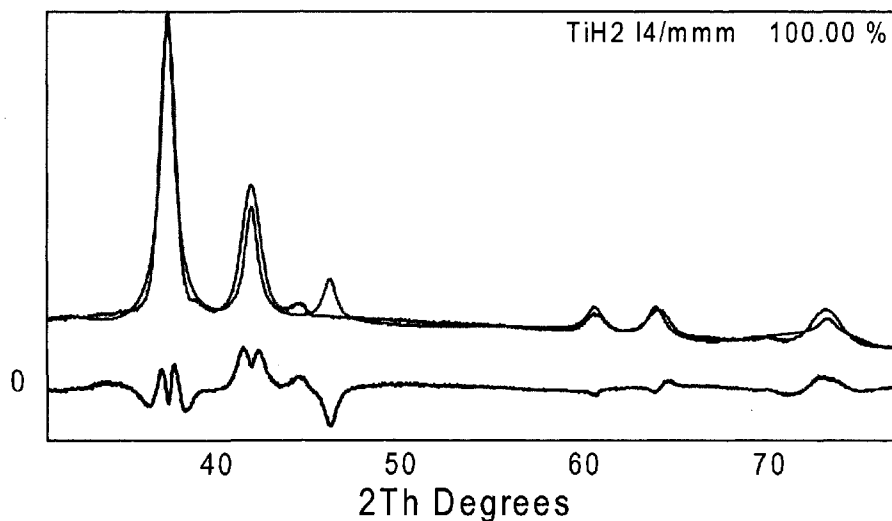


Figure 19. Rietveld full-profile structural refinement of the synchrotron X-ray diffraction pattern of TiH_2 collected at 34 GPa and room temperature. The refinement was carried out using the cubic space group $I4/mmm$ (139). The blue and red lines represent experimental and modeled patterns, respectively. The grey line at the bottom represents the difference between the observed and the refined profile.

The high-pressure phase of TiH_2 is fitted well with a tetragonal structure and displays preferred orientation in the (011) direction as well as line broadening due to non-hydrostatic stresses in the DAC. This lower symmetry structure belongs to the space group $I4/mmm$ (139), with the unit cell parameters: $a = 3.179(2) \text{ \AA}$, $c = 4.309(4) \text{ \AA}$, $V = 43.53(7) \text{ \AA}^3$ and $d = 3.807(65) \text{ g/cm}^3$ (Fig. 19)

The Rietveld refinement of the EDXRD diffraction pattern collected at the highest pressure of this experiment, 34 GPa, is shown in Figure 19. The structure is still

tetragonal, with the unit cell parameters: $a = 3.078(94) \text{ \AA}$, $c = 3.967(12) \text{ \AA}$, $V = 43.53(74) \text{ \AA}^3$ and $d = 3.8070(65) \text{ g/cm}^3$. After decompression to ambient pressure, TiH_2 reverts back to its initial cubic structure, but with a slightly smaller unit cell: $a = 4.400(51) \text{ \AA}$, $V = 88.0(30) \text{ \AA}^3$ and $d = 3.70(13)$.

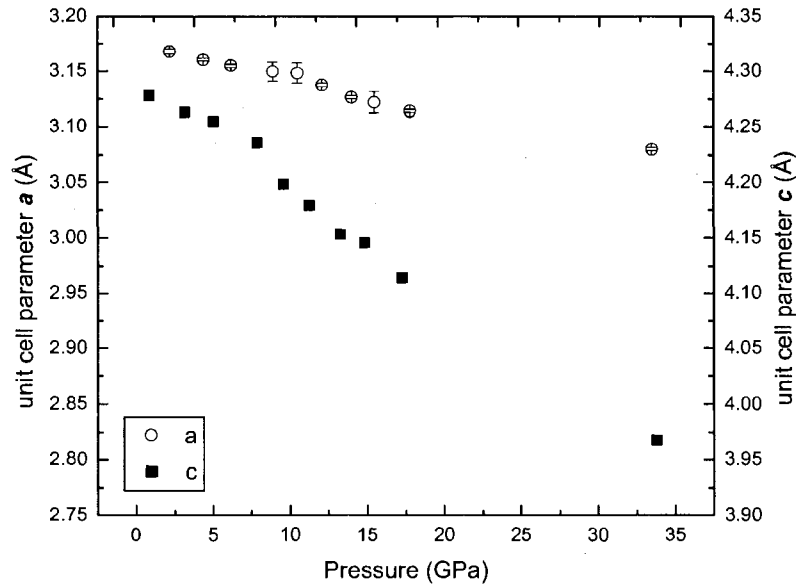


Figure 20. The pressure evolution of the unit cell parameters of the tetragonal phase of TiH_2 compressed from 2.2 to 34 GPa, at room temperature, obtained with the energy dispersive X-ray diffraction. Open circles and the left hand y-axis refer to the parameter a , while the black squares and the right hand y-axis refer to the parameter c .

The demonstrated reversibility of the *cubic* \rightarrow *tetragonal* \rightarrow *cubic* phase transition on compression up to 34 GPa can be interpreted in terms of intrinsic high flexibility of the crystal lattice of TiH_2 . Figure 20 shows the evolution of the unit cell

parameters, of the tetragonal phase of TiH_2 compressed from 2.2 to 34 GPa, at room temperature obtained with the energy dispersive X-ray diffraction technique. The lattice compression is anisotropic, with the c-axis being clearly more compressible than the a-axis. The c/a ratio decreases with pressure from 1.35 at 2.2 GPa to 1.29 at 34 GPa

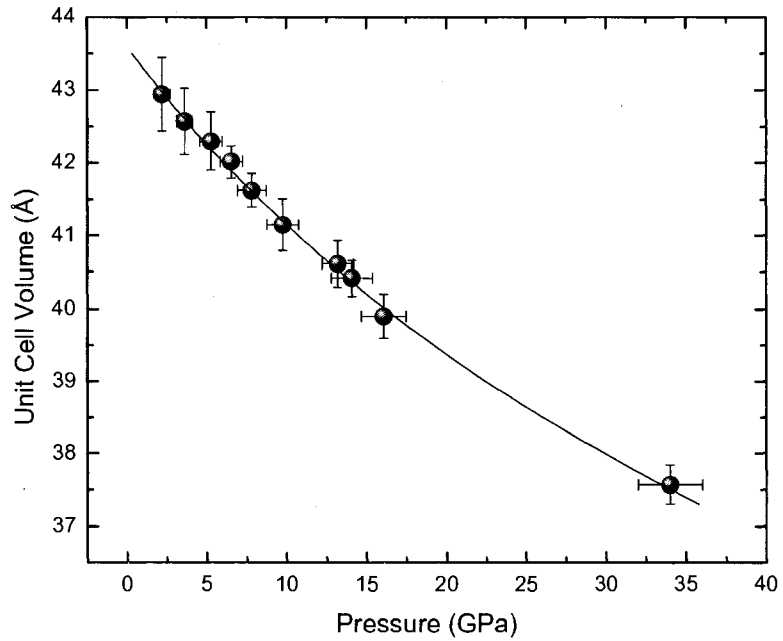


Figure 21. : Unit cell volume of the tetragonal TiH_2 phase as a function of pressure determined from the lattice parameters in the range from 2.2 to 34 GPa. The calculated decrease in the unit cell volume is about 13%. The solid line is the Birch-Murnaghan equation of state fit to the experimental data with $K_0=146(14)$ GPa, $K_0'=6(1)$, $V_0=43.6(0.1)$ Å³.

The pressure evolution of the unit cell volume of the tetragonal phase of TiH_2 on compression to 34 GPa is plotted in Figure 21. The unit cell volume decreases by about 13% ($V/V_0=0.87$, where V_0 is initial cell volume at 2.2 GPa and V is the volume at 34

GPa). on compression up to about 34 GPa. By fitting the pressure-volume data with the third order Birch Murnaghan (see section 5.1.1.) equation of state:

$$P = \frac{3}{2} K_0 \left[\left(\frac{V_0}{V} \right)^{7/3} - \left(\frac{V_0}{V} \right)^{5/3} \right] \left\{ 1 + \frac{3}{2} (K_0' - 4) \left[\left(\frac{V_0}{V} \right)^{2/3} - 1 \right] \right\}$$

we determined the bulk modulus K_0 , its pressure derivative K_0' and the unit cell volume V_0 at ambient conditions of the tetragonal phase of TiH_2 . The following parameters were obtained from the fit: $K_0=146(14)$ GPa, $K_0'=6(1)$, $V_0=43.6$ (0.1) \AA^3 (Fig. 21).

5.1.3. Birch-Murnaghan Equation of State of TiH_2 with ADXRD

The experiments performed with the high-resolution angle-dispersive synchrotron X-ray diffraction (ADXRD) technique show that the cubic lattice of TiH_2 undergoes a pressure-induced phase transformation into the lower symmetry structure at less than 0.6 GPa. TAs mentioned the 0.6 GPa pressure could also be an upper bound for this transition.

A Rietveld full-profile structural refinement of the 0.6 GPa pattern is shown in Figure 22. The high-pressure phase is fitted well with the tetragonal structure, space group $I4/mmm$ (139). The refined unit cell parameters are: $a=3.171(3)$ \AA , $c=4.363(7)$ \AA , $V=43.86(1)$ \AA^3 and X-ray density $d=3.779(9)$ g/cm^3 . The crystal lattice of the new tetragonal phase can be described as a distorted fluorite-type lattice with one crystallographic axis shortened and the two other lengthened. In this structure the H atoms are still situated in tetrahedral interstitial positions within the basic crystal lattice.

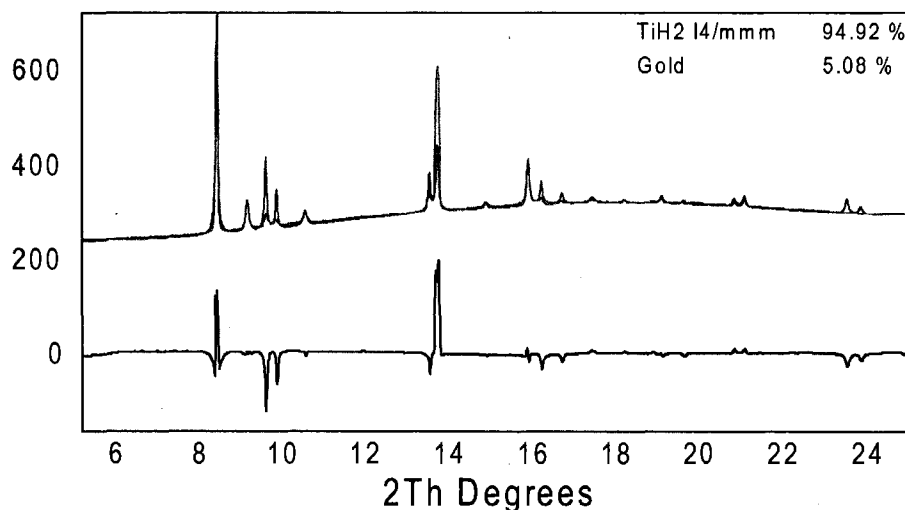


Figure 22. Rietveld full-profile structural refinement of a synchrotron ADXRD pattern of TiH_2 collected *in situ*, at 0.6 GPa and ambient temperature. The refinement was carried out using the tetragonal space group $I4/mmm$ (139). The blue and red lines represent experimental and modeled patterns, respectively. The grey line at the bottom represents the difference between the observed and the calculated peak profiles. The mismatch in intensities is attributed to the large grain size of the sample and the very small x-ray beam size, both of which contribute to reduce the statistics.

The results of the Rietveld refinement of the diffraction pattern collected at 90 GPa is shown in (Figure 23). The structure is still tetragonal, with the unit cell parameters: $a=3.00(2) \text{ \AA}$, $c=3.40(2) \text{ \AA}$, $V=30.6(4) \text{ \AA}^3$ and X-ray density $d=5.42(7) \text{ g/cm}^3$.

After decompression to ambient pressure, a full profile Rietveld structural refinement showed that TiH_2 remains in the tetragonal structure, with: $a=3.1526(4) \text{ \AA}$, $c=4.342(1) \text{ \AA}$, $V=43.16(2) \text{ \AA}^3$ and $d=3.84(1) \text{ g/cm}^3$. This unit cell is slightly smaller than

that of the tetragonal TiH_2 obtained by lowering the temperature instead of increasing pressure.

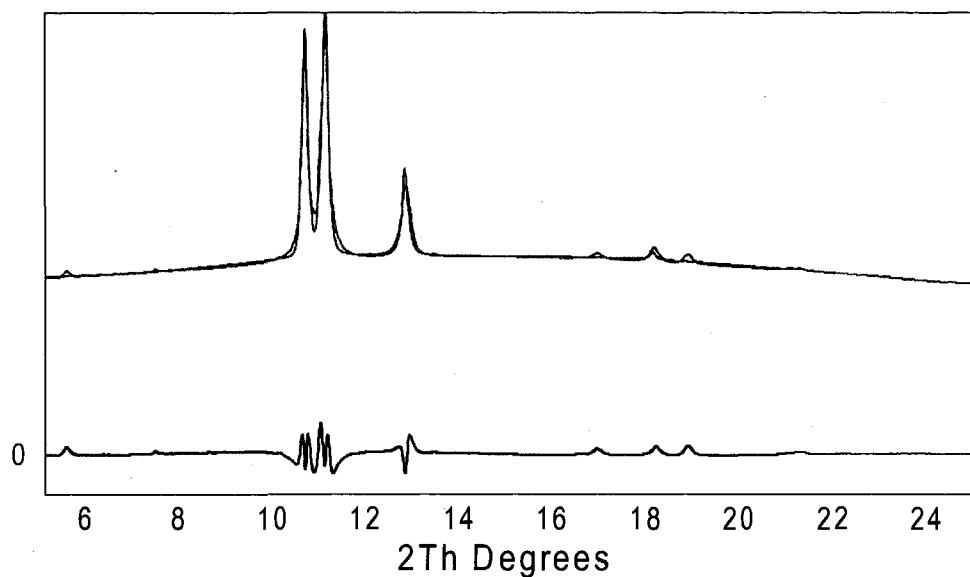


Figure 23. Rietveld full-profile structural refinement of a synchrotron ADXRD pattern of TiH_2 collected *in situ*, at 90 GPa. The refinement was carried out using the tetragonal space group $I4/mmm$ (139). The blue and red lines represent experimental and modeled patterns, respectively. The grey line at the bottom represents the difference between the observed and the calculated peak profiles.

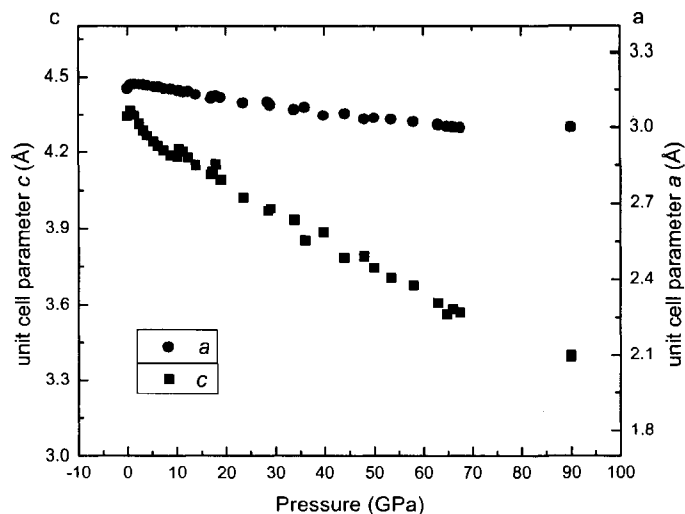


Figure 24. The pressure evolution of the unit cell parameters of the tetragonal phase of TiH_2 compressed from ambient to 90 GPa. Blue circles and the left hand y-axis refer to the parameter a , while the black squares and the right hand y-axis refer to the parameter c . The data between 0.6 GPa and 21 GPa were collected with methanol-ethanol as pressure transmitting medium. The data between 10 GPa and 90 GPa were collected on neat sample. Small differences can be seen between the two datasets: they are not evidence of additional structural rearrangements but are due to the hydrostatic/non-hydrostatic conditions of the two experiments.

In summary, what is important here is that - in contrast to our high-pressure, synchrotron EDXRD investigations of TiH_2 where we observed a reversibility of the *cubic* \rightarrow *tetragonal* \rightarrow *cubic* phase transition on decompression from 34 GPa – the same phase transition is found to be irreversible on decompression from 90 GPa. The irreversibility on decompression down from 90 GPa could be explained in terms of the

compression pressure having reached a critical point beyond which the unit cell is so distorted that it is energetically more favorable for TiH₂ to remain in the tetragonal structure upon decompression to ambient pressure.

In order to follow the pressure evolution of the unit cell parameters, Rietveld full-profile structural refinements were performed on all x-ray diffraction patterns collected. As shown in (Figure 24) the lattice compression of tetragonal TiH₂ is anisotropic, with the c-axis being clearly more compressible than the a-axis. The *c/a* ratio decreases with pressure from 1.376 at 0.6 GPa to 1.320 at 90 GPa. The pressure evolution of the unit cell volume of the tetragonal phase of TiH₂ is shown in Figure 25. Figure 25 clearly demonstrates that there is no large volume discontinuity as TiH₂ undergoes the *cubic* → *tetragonal* phase transition. The transition is direct, without any region where the two phases would co-exist. On compression between 0.6 GPa and 90 GPa the unit cell volume decreases by about 30% ($V/V_0=0.697$, where V_0 is initial cell volume at 0.6 GPa). Using a third order Birch Murnaghan²⁹⁻³³ equation of state we determined the bulk modulus K_0 , its pressure derivative K_0' and the unit cell volume V_0 at ambient conditions of the tetragonal phase of TiH₂. The following parameters were obtained: $K_0=143(7)$ GPa, $K_0'=3.1(1)$, $V_0=44.1(2)$ Å³ (also see Table 2)

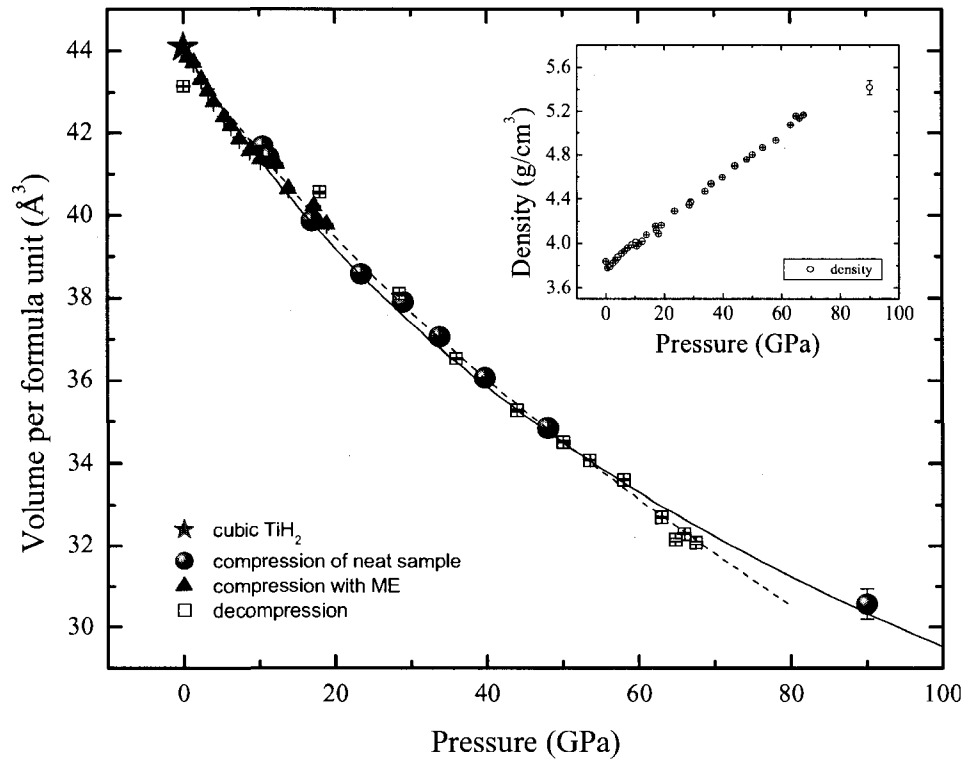


Figure 25. Unit cell volume of the tetragonal TiH_2 phase as a function of pressure on compression from ambient pressure to 90 GPa. The two ADXRD compression runs and the decomposition run are combined in this plot. Triangles indicate the experiments performed with methanol-ethanol as pressure transmitting medium, solid circles represent the experiment carried out without a pressure medium and open squares represent the decompression sequence. The star indicates cubic TiH_2 at ambient pressure. The solid line is the Birch-Murnaghan fit to all the experimental points with $K_0=143(7)$ GPa, $K'_0=3.05(13)$, $V_0=44.1(2) \text{ \AA}^3$. For comparison reasons a second fit was done for all but the 90 GPa point and this fit is shown with a dashed line. The inset shows the pressure evolution of the density of TiH_2 . The decrease in the unit cell volume is about 30% at 90 GPa.

5.1.4. Bulk Modulus of TiH_2 : a Comparison of EDXRD and ADXRD Data.

X-rays interact with the orbital electrons of an atom causing the emission of secondary radiation which becomes the scattered beam. Hence the X-ray scattering power of an atom depends upon the number of electrons of an atom. While the position of metal atoms in metal hydrides is determined by X-ray diffraction, the position of light atoms such as hydrogen cannot be found. In fact, the intensity of the scattered radiation is a function of the square of the scattering amplitude, so the contribution of hydrogen atoms in the XRD pattern of a metal hydride is minute ($\sim 1/100$). Moreover the electron cloud which scatters the X-rays is comparable in size to the wavelength of the radiation, so the scattered wavelets emitted by the electrons will be out of phase with one another causing partial interference thus making the intensity of the scattered radiation less than expected from Z times the single electron intensity.

Since TiH_2 is an interstitial alloy between hydrogen and titanium, and we can only observe diffraction lines due to Ti atoms in X-ray diffraction experiments, it is reasonable to compare our bulk modulus data with those for pure Ti. Such comparison is presented in Table 2. The bulk modulus value of TiH_2 is greater than the bulk modulus of pure Ti metal.⁷³ It should be mentioned that interstitial alloys of transition metals and hydrogen usually exhibit properties which are unlike those of elemental metals, including crystal structure, mechanical properties, as well as very different electronic properties.²⁶ In the case of TiH_2 , the binding energy of Ti is greater than that of Ti in the elemental metal²⁶, what could account for the higher value of bulk modulus of the

hydride found in this experiment. In fact the experimental bulk modulus value found in this work for tetragonal TiH₂ is greater than the bulk modulus of pure Ti metal (Table 2).

Table 2 Summary of bulk moduli, pressure derivatives and ambient pressure volumes, both experimental and theoretical, for TiH₂, Ti and for the super-hard TiO₂ for comparison.

Compound	Experiment/Theory	K ₀ (GPa)	K ₀ '	V ₀ (Å ³)
TiH ₂	EDXRD (this work)	146(14)	6(1)	43.6(1)
	ADXRD (this work)	143(7)	3.1(1)	44.1(2)
	theoretical (this work)	142.6	3.58	–
Ti (hcp)	theoretical (this work)	111	3.73	–
	theoretical (ref. ⁷⁴)	123	–	–
	experimental (ref. ⁷³)	117(9)	3.9(4)	10.66(3)
TiO ₂ rutile	experimental (ref. ⁷⁵)	210	–	–

As a complement to these experimental studies first principle calculations were also carried out ⁷⁶ in order to obtain a theoretical value of the bulk modulus of TiH₂ at 300 K. The calculations yielded a value of K₀=142.6 GPa which is in very good agreement with the experimental bulk modulus reported in this study. The computations also confirmed that at 0.6 GPa the tetragonal structure of TiH₂ is indeed energetically the more favorable one, although the difference in energy with the cubic structure is small. Table 2 illustrates the comparison of the bulk moduli of TiH₂ obtained in the presented

experiments as well as the theoretical value and values for Ti metal and TiO₂ for comparison.

The difference between the values of K_0' between the ADXRD and EDXRD experiments originate from the fact that Bragg reflections of TiH₂ from the EDXRD experiments are much wider, because of the intrinsically lower resolution of the solid state detectors used in EDXRD. This in turn renders structural refinements more challenging, and increases the uncertainty of the lattice parameters and hence of the volume. Also the determination of accurate pressures in the DAC is challenging, particularly in non-hydrostatic experiments. The DAC is an uniaxial stress device⁴³ and without a pressure transmitting medium, in the compression experiments, the pressure gradients in the DAC are significant. In the presented ADXRD study, gold was used as an internal pressure calibrant, and we were able to determine the actual pressure of the portion of the sample being covered by the x-rays, as opposed to reading the pressure of a ruby sphere located on the border of the sample chamber. However, in EDXRD studies we had used only ruby as a pressure indicator, hence the pressures were unavoidably only approximations of the actual pressures in the sample area spanned by the minute synchrotron beam. All the above discussed factors contribute to explain that the resulting EDXRD equation of state differs somewhat from that obtained in the ADXRD experiments.

5.2. Phase Transitions

5.2.1. Types of Phase Transitions

Pressure-driven, solid–solid phase transitions are distinguished as reconstructive or displacive transitions as well as according to their thermodynamic order. Reconstructive phase transitions involve large structural changes, including breaking and forming of bonds. In displacive phase transitions, on the other hand, the positions of the atoms change by small amounts and are often accompanied by small strains. From the thermodynamic point of view the order of the phase transition (first or second) is determined by the order of the derivatives of Gibbs free energy with respect to pressure, which is discontinuous. If the discontinuity appears in the first order derivative:

$$\left. \frac{\partial G}{\partial p} \right|_T = V$$

which means that the volume has a discontinuity, then the phase transition is thermodynamically first order. If the discontinuity is in the second derivative, which is proportional to the compressibility, then the phase transition is of the second order:

$$\left. \frac{\partial^2 G}{\partial p^2} \right|_T = \frac{\partial V}{\partial p} \propto \text{compressibility}$$

There can occur displacive transitions of the first-order with small discontinuities in volume. All reconstructive phase transitions are of the first-order. In the case a transition is strongly of the first order the kinetic barriers which inhibit the transition may be quite large. The transition may then be sluggish, and hysteresis or a larger transition pressure range may be observed on compression than that on

decompression. The thermodynamic equilibrium pressure will be somewhere in between those two pressures and is often arbitrarily set to the middle point. Hysteresis decreases at high temperatures so the equilibrium pressure may be pinpointed in this way.

5.2.2. Titanium Hydride

The pressure evolution of the unit cell volume of TiH_2 from ambient pressure up to 90 GPa is shown in Figure 25. The lone star marks the ambient pressure point, which is the only pressure where the cubic phase was observed. In the entire experimental pressure range, only one pressure-induced phase transition is observed, at 0.6 GPa. It should be pointed out that the pressure evolution of the unit cell volume of TiH_2 for the experiments performed with methanol-ethanol to 21 GPa as well as for those performed without a pressure transmitting medium up to 90 GPa does not present any striking differences. There is no readily apparent volume discontinuity as TiH_2 undergoes the cubic to tetragonal phase transition. Also the transition is direct, without any region where the two phases would co-exist. Because of the lack of discontinuity in the pressure-volume plots for both the EDXRD and ADXRD we believe that the phase transition is of the second order. Based on these observations the author believes that shear stresses in the DAC do not play a significant role in driving the cubic to tetragonal phase transition in TiH_2 . Moreover the distortion of the ambient pressure, face center cubic crystal lattice into a face centered tetragonal lattice (which is a distorted cubic structure) with one axis elongated and two shortened also points towards a displacive phase transition.

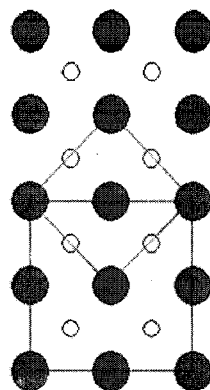


Figure 26. A simplistic model of the non-isomorphic subgroup relation of the tetragonal space group 139 (green) to the cubic space group 225 (red).

Figure 26 explains how to generate the structure of the high-pressure tetragonal phase (SG 139, green unit cell in [001]) from the ambient pressure cubic phase (SG 225, red unit cell in [001]). Figure 26 provides indirect evidence for the observed phase transformation, since SG 139 is a non-isomorphic subgroup of SG 225. Therefore, only minor structural rearrangements are needed to synthesize the high-pressure phase. This might explain the reversible nature of the phase transformation at lower pressure (34 GPa) since activation energy is presumably low, but somehow significantly increases after decompression from very high pressure (90 GPa). The irreversibility on decompression down from 90 GPa could be explained in terms of the compression pressure having reached a critical point beyond which the unit cell is so distorted that it is energetically more favorable for TiH_2 to remain in the tetragonal structure upon decompression to ambient pressure.

5.2.3. Phase Diagram of TiH_2

Based on the results obtained in this work for both the temperature and the pressure-variable data sets, a tentative phase diagram can be proposed for TiH_2 (Figure 27).

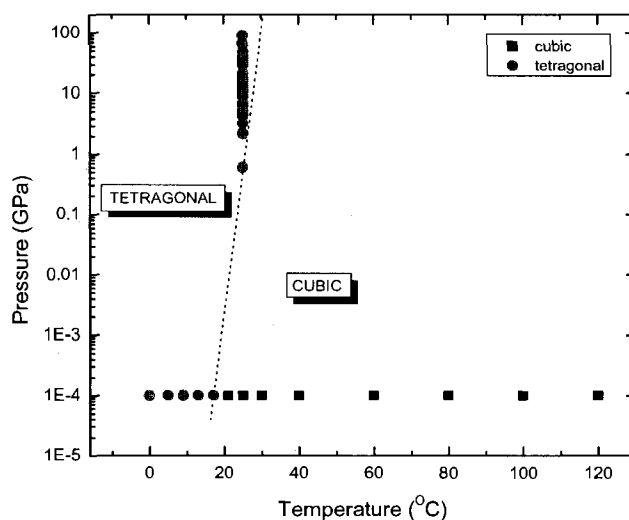


Figure 27. Phase diagram of TiH_2 based on experimental results of this work. Black squares represent the cubic structure while red circles represent the tetragonal structure of TiH_2 .

5.3. ADXRD versus EDXRD

In these high-pressure investigations of TiH_2 , the author carried out X-ray diffraction experiments in two different modes: the angle dispersive mode and the energy dispersive mode.

EDXRD uses polychromatic X-rays and a fixed detector angle. In this case the Bragg equation may be rewritten as:

$$\lambda = \frac{hc}{E} = 2d_{hkl}\sin\theta$$

Diffraction patterns are collected at a fixed detector angle and as a function of energy. Progress in this technique has been linked with the development of solid state germanium detectors. These detectors offer a wide energy range, up to several tens of keV. Silicon solid state detectors can be used in the range of 20-30 keV. Solid state detectors offer the advantage of a fast data collection. Disadvantages are an intrinsically lower resolution as well as a need for frequent recalibration with fluorescence lines of some elements. Fluorescence of the sample being investigated can also appear on the diffraction patterns if the absorption edge is in the energy range used for diffractions studies and a Ge detector is used. They can be distinguished from diffraction lines because their position is virtually independent of pressure and of the detector angle.

ADXRD uses a monochromatic beam and a two-dimensional detector: flat (or cylindrical) imaging-plate detectors or alternatively flat CCD detectors. The collected patterns are two-dimensional Debye-Scherrer images (rings), which need to be extracted into one-dimensional diffraction patterns in order to be analyzed. The key advantage of ADXRD over EDXRD can be substantially better resolution. The limitation on resolution for 2D detectors is the pixel size (several tens of microns) but this can be improved by increasing the sample to detector distance. Since the Debye-Scherrer diffraction cones increase in size with distance, two adjacent cones become more separated at longer distance. Data from ADXRD are suitable for Rietveld analysis. In addition if one uses a pressure standards, its diffraction lines will be better resolved, thus allowing for a better determination of pressure.

The superiority of ADXRD as compared to EDXRD can be seen very well in the results presented in this work. The reflections due to TiH_2 are much better resolved with ADXRD and have narrower bandwidths. Moreover, the Rietveld refinements of ADXRD data are of better quality and with smaller uncertainties. In this work the combination of the ADXRD technique with a very large pressure scale (0-90 GPa) allowed the author to obtain a superior equation of state for TiH_2 as compared to that of EDXRD data.

5.4. Issues: Texture, Pressure-Transmitting Media and Pressure.

5.4.1. Preferred Orientation

The pressure medium serves to transform uniaxial force in the DAC into a quasi-hydrostatic pressure. Under uniaxial forces nonspherical microcrystallites have a tendency to align with their long axes perpendicular to the cell axis. As a result of this preferred orientation the intensities of diffraction lines can be considerably modified. Texture is a common issue in high-pressure x-ray diffraction measurements of powdered samples. Since the force in a DAC is essentially uniaxial, any nonspherical crystallites will likely align with their long axis perpendicular to the cell axis.³⁹ As a consequence of the preferred crystallite orientation, the intensities of diffraction lines can sometimes be greatly altered (Figure 28). In addition, in the present experiments the crystallite size was relatively large as compared to the beam size which further reduced the statistics of the measurement as well as contributed to further enhance the altered intensities in the diffraction peaks because of preferred orientation effects.

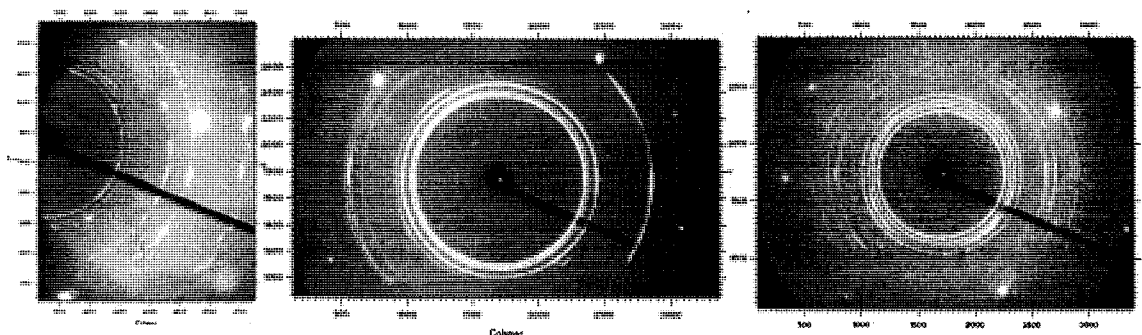


Figure 28. ADXRD patterns collected with the image plate detector. Ambient pressure, 90 GPa and after decompression, from left to right, respectively. Texture due to preferred orientation is clearly visible on the leftmost picture. Texturing was eliminated to some extent by moving over a small sample area during collection (center and right).

In the high-pressure experiments carried out by the author preferred orientation and/or crystallite size is very apparent (Fig. 28). In the Debye-Scherrer configuration the diffraction pattern should consist of uniform rings since the crystallites are randomly dispersed in the powdered sample. Instead the rings appear very spotty. An additional reason, besides preferred orientation, is the poor statistics due to the fact that in the very small sample chamber only a small number of crystallites can be placed. Therefore, there is only a small number of crystallites in the path of the X-rays and as they assume a preferred orientation under pressure this results in a spotty diffraction pattern. In the presented experiments, the image plate statistics was improved by scanning over the sample in the vertical and horizontal directions while the patterns were being acquired. This resulted in a decrease of spottiness of the diffraction rings. Concluding, in the

presented investigations texture contributes to explain the somewhat altered intensity profiles of the diffraction patterns as they appear in the Rietveld structural refinements.

5.4.2. On Successfully Achieving Extreme Pressures

It has to be pointed out that beyond about 20 GPa high-pressure studies become much more difficult to carry out successfully, and exponentially more difficult past ~50 GPa. When pressures of the order of a mega bar are desired, the careful and extremely precise preparation of the DAC becomes crucial because of the brittleness of diamond. This includes the need for achieving a perfect parallelism of the two diamond culets, which should also have equal coincident diameters, perfect vertical alignment of the culets, combined with a specific thickness of the gasket and a circular (as opposed to oval) sample chamber. At pressures of the order ~80 GPa, anvil failure is a distinct possibility.^{46, 47} If the sample chamber is not perfectly spherical and diamond parallelism is not insured, then as soon as the pressure is applied, the sample chamber will move and flow to one side, pushed by the diamonds, resulting in gasket rupture followed by anvil failure as the two diamonds come into sudden contact. If signs of gasket flow are detected (such as change in the shape of sample chamber or loss of pressure indicating that the pressure medium escaped) it is usually better to halt the experiment to preserve diamonds.

In a DAC pressure is increased by tightening screws between two parts of the cell in order to apply load to the washers. Pressure increase in the sample chamber is usually not a linear process: it is slow at lower pressure and becoming faster as pressure is increased. The experimenter has to decide how much to turn the screws (1/8, 1/16 of

a turn etc) and turn screws at the same time and at an identical rate in order to insure that pressure increases as uniformly as possible so that the sample chamber will remain stable. At the same time, however, turning of the screws becomes more and more difficult as pressure increases and greater manual force has to be exerted. In summary, at pressures above 30 GPa or so increasing pressure to a desired value becomes something between art and exercise in manual skill.

In the presented series of high-pressure experiments, compression of TiH_2 was successfully achieved up to 90 GPa with only a minor impact to one of the anvils, and a decompression run to ambient pressure was carried out as well. The advantage of carrying out structural studies up to almost a mega bar lies in the fact that the equation of state of TiH_2 can be determined with much more confidence when such an extensive pressure range is available for the fit of the equation of state.

5.4.3. The Quest for Hydrostatic Conditions and Measuring Accurate Pressures.

The diamond anvil cell is basically an uniaxial stress device and truly hydrostatic conditions are only obtained when the sample is contained within a fluid pressure medium.⁴³ The pressure-transmitting medium serves to transmit a uniform pressure to the sample and to the pressure indicator. A commonly used medium is a 4:1 mixture of methanol-ethanol. As long as the medium remains fluid, the pressure conditions will be hydrostatic. As pressure increases however all media undergo solidification and the stress in the pressure chamber induces strong nonhydrostatic components and some inhomogeneity. This can affect the behavior of the studied material and impact the diffraction patterns. Known pressure media, such as N_2 , He or Ar increase the pressure

range where conditions remain quasi-hydrostatic.^{46, 47} At ambient temperature, a completely hydrostatic environment cannot be sustained above 13 GPa due to solidification and/or stress in all known pressure media.^{77, 78} Recently however it was found that solidified helium maintains a good degree of hydrostaticity up to at least 50 GPa.⁷⁹

The ruby pressure scale, is based on a fluorescence line (R_1) which shifts with pressure almost linearly up to 10 GPa, with $dp/d\lambda=0.2746$ GPa Å⁻¹, and with a small deviation at higher pressures, according to the empirical equation⁴⁸ :

$$P(\text{GPa}) = \frac{1904}{B} \left[\left(1 + \frac{\Delta\lambda}{\lambda_0} \right)^B - 1 \right]$$

where $B=7.665$ for quasi-hydrostatic conditions and $B=5.0$ for non-hydrostatic conditions.

What is the accuracy in pressure measurements when using the ruby scale? The accuracy changes depending on how high-pressure is considered: acceptable accuracy is ~0.1 GPa up to ~10 GPa, then between 0.5 and 1 GPa at pressures of a few tens of GPa. The actual accuracy is not only limited by the accuracy of the primary pressure scale but also by the spectral resolution of the R_1 ruby line. At about 100 GPa the diamond fluorescence contributes and also the intensity of the R_1 line is reduced which decreases the resolution significantly. Also below 1 GPa the sensitivity of the ruby scale is poor. According to Holzapfel *et al.*⁸⁰ accounting for all the factors the accuracy of the measurement of pressure with the secondary ruby scale is ~1% up to ~10 GPa and ~3% at around 100 GPa.

Non-hydrostatic stresses do not have to be seen as a weakness, since they can also be used in exploring the elastic properties of media. The effect of nonhydrostatic stress on the structural stability of high-pressure phases is a relatively unexplored field.³⁹ Non-hydrostatic conditions can favor some transitions and transition pressures can be influenced by the degree of hydrostaticity.⁴⁰

With the absence of a pressure transmitting medium, in the compression experiments the pressure gradients in the DAC are significant. All components and contents of a pressure cell are strained and peaks from a strained sample or pressure indicator exhibit line broadening which also depends on temperature.⁴⁰

With the use of gold as an internal pressure calibrant, dispersed within the sample, we were able to determine the actual pressure of that portion of the sample which was directly in the path of the X-rays, as opposed to the pressure experienced by a ruby microsphere placed more radially outward with respect to the sample. It is customary to spread the ruby pressure marker in the sample chamber so that its reflections will not contribute to the XRD pattern of the investigated sample, since that would make the structural refinement more complex. In the EDXRD studies^{52, 81} we used only ruby as pressure indicator hence the pressures were unavoidably only approximates of the actual pressures and therefore the resulting equation of state differs somewhat from that obtained in this work.

The accuracy of pressure measurements when using the equation of state of a metal depends on how well the reflections corresponding to the metal can be fitted.

Also, the width of the reflections, which is influenced by non-hydrostaticity in the DAC will in turn influence how good a pressure reading can be made.

At the highest pressure achieved in this work, 90 GPa, it is estimated that the accuracy in the measurement of pressure is of about ± 2 GPa only due to the non-hydrostatic conditions of the experiment, which caused considerable line broadening.

5.5. Conclusions

Temperature-dependent, conventional, angle-dispersive x-ray diffraction studies, as well as pressure-dependent, synchrotron radiation-based, energy-dispersive and high-resolution angle-dispersive x-ray diffraction studies of TiH_2 were performed. The endeavor was to probe the effect of temperature on one side, and the effect of high-pressure compression on the other side, on the compound's structure. The goal was to reveal any pressure-induced structural transformations that may occur in the cubic lattice of TiH_2 .

The temperature evolution of the x-ray diffraction patterns was followed in the range from 0°C to 120°C at ambient pressure. A *cubic* \rightarrow *tetragonal* phase Jahn-Teller phase transition in TiH_2 was observed at about 17°C . It was also found that cubic TiH_2 does not undergo any phase transition up to at least 120°C .

In the first series of high-pressure studies, the structure of TiH_2 was followed *in situ* (diamond anvil cell), with EDXRD on compression from ambient pressure up to 34 GPa and on consecutive decompression. With pressure increase to 2.2 GPa a phase transition from cubic to tetragonal structure was observed. Moreover, compression

above 2.2 GPa of the tetragonal phase of TiH_2 revealed anisotropic lattice compression, with the c -axis being more compressible than the a -axis. The pattern of TiH_2 quenched from 34 GPa to ambient conditions indicated that the pressure-induced reconstructive modification was completely reversible upon decompression. The structure of the pressure-quenched material was identical to that of the initial cubic TiH_2 , but with a slightly smaller unit cell. The pressure-volume data of the tetragonal phase of TiH_2 were analyzed using the third order Birch-Murnaghan equation of state and yielded a zero pressure bulk modulus $K_0 = 146(14)$ GPa and a pressure derivative of $K_0' = 6(1)$.

In the second series of high-pressure studies, the structure of TiH_2 was followed *in situ* (diamond anvil cell), with high-resolution ADXRD on compression from ambient pressure up to 90 GPa and on consecutive decompression. The endeavor was to pinpoint the phase transition pressure observed with the low resolution EDXRD technique. The goal was also to probe the effect of high-pressure compression on the compound's structure and to study the equation of state of TiH_2 into the megabar region. The cubic (*fcc*) to tetragonal (*fct*) phase transition was observed at 0.6 GPa in quasi-hydrostatic conditions. In analogy to what was observed with EDXRD, the lattice compression was anisotropic with the c parameter being clearly more compressible than the a parameter. The tetragonal structure persisted up to the highest investigated pressure, 90 GPa. TiH_2 quenched from 90 GPa to ambient pressure conditions indicated that the pressure-induced, displacive modifications, corresponding to a phase transition, were irreversible and upon decompression, the high-pressure tetragonal phase was preserved. The pressure-volume data of the tetragonal phase of TiH_2 analyzed using the

third order Birch-Murnaghan equation of state, yielded a zero pressure bulk modulus $K_0 = 143$ (7) GPa and a pressure derivative of $K'_0 = 3.0$ (1), confirmed by first-principle calculations which yielded $K_0 = 142.6$ GPa.

There is no readily apparent volume discontinuity as TiH_2 undergoes the *cubic* \rightarrow *tetragonal* phase transition. Also the transition is direct, without any region where the two phases would co-exist. Due to the lack of discontinuity in the pressure-volume data for both the EDXRD and ADXRD, it is believed that the observed phase transition is of the second order. Based on these arguments the author believes that shear stresses in the DAC do not play a significant role in driving the cubic to tetragonal phase transition in TiH_2 .

In fact, in order to generate the high-pressure tetragonal phase of TiH_2 from its ambient pressure cubic phase, only minor structural rearrangements are needed, because the space group of the tetragonal phase is a non-isomorphic subgroup of the space group of the cubic phase. This also contributes to explain the reversible nature of the phase transformation on compression to 34 GPa, since the activation energy for this transition is presumably low. The irreversibility of the phase transition upon decompression down from 90 GPa could be explained in terms of the compression pressure having reached a critical point beyond which the unit cell is distorted to such extent that it is energetically more favorable for TiH_2 to remain in the tetragonal structure.

REFERENCES

- 1 United States Department of Energy, Office of Basic Energy Sciences DOE
Hydrogen Program: Science <http://www.hydrogen.energy.gov/science.html>
(2007)
- 2 G. Sandrock, A panoramic overview of hydrogen storage alloys from a gas
reaction point of view, *J. Alloys Compd.* 293-295, 877 (1999).
- 3 L. Schlapbach and A. Züttel, Hydrogen-storage materials for mobile applications.,
Nature 414, (2001).
- 4 R. J. Hemley, Effects of High Pressure on Molecules, *Annual Review of Physical
Chemistry* 51, 763 (2000).
- 5 R. J. Hemley and N. Ashcroft, The revealing role of pressure in the condensed
matter sciences, *Physics Today* 51/8, 26 (1998).
- 6 G. Sandrock, K. Gross, and G. Thomas, Effect of Ti-catalyst content on the
reversible hydrogen storage properties of the sodium alanates, *J. Alloys Compd.*
339, 299 (2002).
- 7 P. Wang, X. D. Kang, and H. M. Cheng, Exploration of the Nature of Active Ti
Species in Metallic Ti-Doped NaAlH₄, *J. Phys. Chem. B* 109, 20131
(2005).
- 8 A. Borgschulte, R. J. Westerwaal, J. H. Rector, H. Schreuders, B. Dam, and R.
Griessen, Catalytic activity of noble metals promoting hydrogen uptake, *Journal
of Catalysis* 239, 263 (2006).
- 9 T. Tanaka, M. Keita, and D. E. Azoneifa, Theory of hydrogen absorption in metal
hydrides, *Phys. Rev., B, Condens, Matter Mater. Phys.* 24, (1981).
- 10 G. G. Libowitz, *The Solid-State Chemistry of Binary Metal Hydrides* (W. A.
Benjamin, Inc., New York, NY, 1965).
- 11 W. M. Mueller, J. P. Blackledge, and G. G. Libowitz, *Metal Hydrides* (Academic
Press, Inc., New York, NY, 1968).
- 12 L. Schlapbach ed., *Hydrogen in Intermetallic Compounds* (Springer-Verlag, Berlin
Heidelberg, 1988).
- 13 L. N. Padurets, Z. V. Dobrokhotova, and A. L. Shilov, Transformations in titanium
dihydride phase, *Int. J. Hydrog. Energy* 24, 153 (1999).
- 14 M. Slaman, B. Dam, M. Pasturel, D. M. Borsa, H. Schreuders, J. H. Rector, and R.
Griessen, Fiber optic hydrogen detectors containing Mg-based metal hydrides,
Sensors and Actuators B 123, 538 (2007).
- 15 X. Yao, C. Wu, A. Du, G. Q. Lu, H. Cheng, S. C. Smith, J. Zou, and Y. He, Mg-Based
Nanocomposites with High Capacity and Fast Kinetics for Hydrogen Storage, *J.
Phys. Chem. B* 110, 11697 (2006).

- 16 G. Sandrock, J. Reilly, J. Graetz, Wei-Min Zhou, J. Johnson, and J. Wegrzyn, Alkali metal hydride doping of α -AlH₃ for enhanced H₂ desorption kinetics, *J. Alloys Compd.* 421, 185 (2006).
- 17 D. Kyoï, et al., A new ternary magnesium–titanium hydride Mg₇TiH_x with hydrogen desorption properties better than both binary magnesium and titanium hydrides., *J. Alloys Compd.* 372 213 (2004).
- 18 H. Leng, T. Ichikawa, and H. Fujii, Hydrogen storage properties of Li-Mg-N-H systems with different ratios of LiH/Mg(NH₂)(₂), *J. Phys. Chem. B* 110, 12964 (2006).
- 19 Z. Lodziana and T. Vegge, Structural stability of complex hydrides: LiBH₄ revisited, *Phys. Rev. Lett.* 93, 4 (2004).
- 20 S. Shi and J.-Y. Hwang, Research frontier on new materials and concepts for hydrogen storage, *Int. J. Hydrog. Energy* 32, 224.
- 21 T. Ichikawa, N. Hanada, S. Hino, and H. Fujii, Remarkable improvement of hydrogen sorption kinetics in magnesium catalyzed with Nb/₂O/₅, *J. Alloys Compd.* 420, 46 (2006).
- 22 P. Vajeeston, P. Ravindran, B. C. Hauback, H. Fjellvag, A. Kjekshus, S. Furuseth, and M. Hanfland, Structural stability and pressure-induced phase transitions in MgH/₂, *Phys. Rev., B, Condens. Matter Mater. Phys.* 73, 224102 (2006).
- 23 L. Zaluski, A. Zaluska, and J. O. Strom-Olsen, Nanocrystalline magnesium for hydrogen storage *J. Alloys Compd.* 288, 217 (1999).
- 24 T. Yildirim, J. Íñiguez, and S. Ciraci, Molecular and dissociative adsorption of multiple hydrogen molecules on transition metal decorated C₆₀, *Phys. Rev., B, Condens. Matter Mater. Phys.* 72, 153403 (2005).
- 25 R. Strobel, J. Garche, P. T. Moseley, L. Jorissen, and G. Wolf, Review: Hydrogen storage by carbon materials, *Journal of Power Sources* 159, 781 (2006).
- 26 J. H. Weaver, D. J. Peterman, D. T. Peterson, and A. Franciosi, Electronic structure of metal hydrides. IV. TiH/_x, ZrH/_x, HfH/_x, and the FCC-FCT lattice distortion, *Phys. Rev. B, Condens. Matter* 23, 1692 (1981).
- 27 K. Nobuhara, H. Kasai, W. A. Dino, and H. Nakanishi, H₂ dissociative adsorption on Mg, Ti, Ni, Pd and La Surfaces, *Surface Science* 566-568, 703 (2004).
- 28 B. Bogdanovic and M. Schwickardi, *J. Alloys Compd.* 253-254, 1 (1997).
- 29 B. Farangis, P. Nachimuthua, T. J. Richardson, J. L. Slack, B. K. Meyer, R. C. C. Perera, and M. D. Rubin, Structural and electronic properties of magnesium–3D transition metal switchable mirrors, *Solid State Ionics* 165 309 (2003).
- 30 J. Iniguez, T. Yildirim, T. J. Udovic, M. Sulic, and C. M. Jensen, Structure and hydrogen dynamics of pure and Ti-doped sodium alanate, *Phys. Rev., B, Condens. Matter Mater. Phys.* 70, 60101 (2004).
- 31 C. Kittel, *Intorduction to Solid State Physics* (John Wiley & Sons, New York, 1996).
- 32 H. Ibach and H. Luth, *Solid State Physics* (Springer-Verlag Berlin Heidelberg, 1996).
- 33 P. Atkins, *Physical Chemistry* (Oxford University Press, 1998).
- 34 T. Hartmann (private communication).

- 35 D. Attwood, *Soft X-rays and Extreme Ultraviolet Radiation* (Cambridge University Press, New York, NY, 2000).
- 36 M. R. Wehr, J. A. Richards, and T. W. Adair, *Physics of the Atom* (Addison-Wesley Publishing Company, Reading, MA, 1978).
- 37 K. Kirschner, *Einführung in die Röntgenfeinstrukturanalyse* (Veiweg, Braunschweig/Wiesbaden, 1987).
- 38 K. N. Trueblood, H.-B. Burgi, H. Burzlaff, D. Dunitz, C. M. Gramaccioli, H. H. Schulz, U. Shmueli, and S. C. Abrahams, Atomic Displacement Parameter Nomenclature: Report of a Subcommittee on Atomic Displacement Parameter Nomenclature., *Acta Crystallographica A* 52, 770 (1996).
- 39 A. Mujica, A. Rubio, A. Muñoz, and R. J. Needs, High-pressure phases of group-IV, III-V, and II-VI compounds, *Reviews of Modern Physics* 75, 863 (2003).
- 40 W. Paszkowicz, *X-Ray Diffraction at the Turn of the Century*, (2002).
- 41 B. Buras, J. S. Olsen, L. Gerward, G. Will, and E. Hinze, X-ray energy-dispersive diffractometry using synchrotron radiation *Journal of Applied Crystallography* 10, 431 (1977).
- 42 E. Wigner and H. B. Huntington, *J. Chem. Phys.*, 764 (1935).
- 43 A. Jayaraman, Diamond anvil cell and high-pressure physical investigations, *Reviews of Modern Physics* 55, 65 (1983).
- 44 J. C. Jamieson, A. W. Lawson, and N. D. Nachtrieb,, *Rev. Sci. Instrum.* 30, 1016 (1959).
- 45 C. E. Weir, E. R. Lippincott, A. van Valkenburg, and E. N. Bunting, *J. Res. Natl. Bur. Stand.* 63, 55 (1959).
- 46 M. I. Eremets, *High-Pressure Experimental Methods* (Oxford University Press, Oxford, 1996).
- 47 W. B. Holzapfel, Isaacs N. S. , *High-Pressure Techniques in Chemistry and Physics* (Oxford University Press, Oxford/New York/Tokyo, 1997).
- 48 H. K. Mao, in *Simple Molecular Systems at Very High Density*, edited by A. Polian, P. Loubeyre and N. Boccara (Plenum, New York, 1989), p. 221.
- 49 R. J. Hemley ed., *Ultrahigh-Pressure Mineralogy: Physics and Chemistry of the Earth Deep Interior* (The Mineralogical Society of America, Washington, DC, 1998).
- 50 G. Margaritondo, *Introduction to synchrotron radiation* (Oxford University Press, New York, 1988).
- 51 U.S. Department of Energy, Office of Science, Office of Basic Energy Sciences, National Synchrotron X-ray Research Facility, Advanced Photon Source <http://www.aps.anl.gov/> (2008)
- 52 P. E. Kalita, A. L. Cornelius, K. E. Lipinska-Kalita, C. L. Gobin, and H. P. Liermann, In situ Observations of Temperature- and Pressure-Induced Phase Transitions in TiH₂: Angle-Dispersive and Synchrotron Energy-Dispersive X-ray Diffraction Studies, *Journal of Physics and Chemistry of Solids*, (to be published).
- 53 H. K. Mao, P. M. Bell, J. W. Shaner, and e. al., *J. Appl. Phys.* 49, 3276 (1978).
- 54 W. Kraus and G. Nolze, *Powder Cell 2.4* (Federal Institute for Materials Research and Testing, 12489, Berlin, Germany).

55 Bruker-AXS, *Topas*.
 56 A. Hammersley, *Fit2D* V12.077 (ESRF, Grenoble, France, 1987-2005).
 57 H. K. Mao, P. M. Bell, J. W. Shaner, and D. J. Steinberg, Specific volume
 measurements of Cu, Mo, Pd, and Ag and calibration of the ruby $R/\text{sub } 1/$
 fluorescence pressure gauge from 0.06 to 1 Mbar, *J. Appl. Phys.* 49, 3276 (1978).
 58 O. L. Anderson, D. G. Isaak, and S. Yamamoto, Anharmonicity and the Equation
 of State for Gold, *J. Appl. Phys.* 65, 1534 (1989).
 59 Bruker-AXS, *Topas* 3.2 (Bruker, Karlsruhe, Germany, 2006).
 60 Patricia-FIGURE.
 61 A. San-Martin and F. D. Manchester, The H-Ti (hydrogen-titanium) system,
 Bulletin of Alloy Phase Diagrams 8, 30 (1987).
 62 F. D. Murnaghan, The Compressibility of Media Under Extreme Pressures,
 Proceedings of the National Academy of Sciences of the United States 30, 244
 (1944).
 63 F. D. Murnaghan, *Finite Deformation of an Elastic Solid* (Wiley, New York, 1951).
 64 A. E. H. Love, *A Treatise on the Mathematical Theory of Elasticity* (Cambridge
 University Press, Cambridge, 1927).
 65 F. D. Stacey, B. J. Brennan, and R. D. Irvine, Finite strain theoried and
 comparisons with seismological data. , *Geophysical Surveys* 4, 189 (1981).
 66 J. Hama and K. Suito, *J. Phys.: Condens. Matter* 8, 67 (1996).
 67 A. M. Hofmeister, *Geophys. Res. Lett.* 20, 635 (1993).
 68 W. B. Holzapfel, *Rep. Prog. Phys.* 59 29 (1996).
 69 J.-P. Poirier and A. Tarantola, A logarithmic equation of state, *Physics of Earth
 and Planetary Interiors* 109, 1 (1998).
 70 W. B. Holzapfel, Equations of State for solids under strong compression, *High
 Pressure Research* 16, 81 (1998).
 71 R. Rydberg, Graphische Darstellung einiger bandenspektroskopischer
 Ergebnisse., *Z. Phys.* 73, 376 (1932).
 72 P. Vinet, J. Ferrante, J. Smith, and J. Rose, A universal equation of state for solids,
Phys C: Solid State 19, L467 (1986).
 73 D. Errandonea, Y. Meng, M. Somayazulu, and D. Hausermann, Pressure-induced
 alpha rarr omega transition in titanium metal: a systematic study of the effects
 of uniaxial stress, *Physica B* 355, 116 (2005).
 74 Y. Z. Nie and Y. Q. Xie, Ab initio thermodynamics of the hcp metals Mg, Ti, and Zr,
Phys. Rev. B 75, 7 (2007).
 75 E. Francisco, Spinodal equation of state for rutile TiO_2 , *Phys. Rev., B, Condens,
 Matter Mater. Phys.* 67, (2003).
 76 P. E. Kalita, S. V. Sinogeikin, K. E. Lipinska-Kalita, T. Hartmann, X. Ke, C. Chen, and
 A. L. Cornelius, Equation of State of TiH_2 up to 90 GPa: a High-Resolution
 Synchrotron X-Ray Diffraction Study., *Physical Reviev B*, (submitted).
 77 T. S. Duffy, S. Guoyin, D. L. Heinz, S. Jinfu, M. Yanzhang, M. Ho-Kwang, R. J.
 Hemley, and A. K. Singh, Lattice strains in gold and rhenium under
 nonhydrostatic compression to 37 GPa, *Phys. Rev. B, Condens. Matter* 60, 15063
 (1999).

- 78 P. Loubeyre, R. LeToullec, D. Hausermann, M. Hanfland, R. J. Hemley, H. K. Mao,
and L. W. Finger, X-ray diffraction and equation of state of hydrogen at megabar
pressures, *Nature* 383, 702 (1996).
- 79 K. Takemura, Evaluation of the hydrostaticity of a helium-pressure medium with
powder x-ray diffraction techniques, *J. Appl. Phys.* 89, 662 (2001).
- 80 W. B. Holzapfel, M. Hartwig, and W. Sievers, Equations of State for Cu, Ag, and
Au for Wide Ranges in Temperature and Pressure up to 500 GPa and Above, *J.*
Phys. Chem. Ref. Data 30, 515 (2001).
- 81 P. E. Kalita, A. L. Cornelius, H. P. Liermann, and W. Yang, in *Fifth International
Conference on Synchrotron Radiation in Materials Science, SRMS-5*, Chicago, IL,
USA, 2006).

VITA

Graduate College
University of Nevada Las Vegas

Patricia E. Kalita

Home Address:

2180 E. Warm Springs Rd.
Las Vegas, Nevada, 89119

Degrees:

Bachelor of Sciences, Physics, 2005
University of Nevada Las Vegas

Baccalauréat Scientifique, 1999
Lycée Louis le Grand, Paris, France

Publications:

- P. E. Kalita, S. Sinogeikin, K. Lipinska-Kalita, T. Hartmann, X. Ke, C. Chen and A. Cornelius: Equation of State of TiH_2 to 90 GPa, Phys. Rev. B, submitted (2008)
- P. E. Kalita, A. Cornelius, K. Lipinska-Kalita, C. L. Gobin and H. P. Liermann: EDXRD investigation of TiH_2 to 34 GPa, J. Phys. Chem. Solids, submitted (2008)
- K. E. Lipinska-Kalita, P. E. Kalita, O. A. Hemmers, R. J. Hemley and G. Mariotto, Structural Transformations and Equation of State of a Nanocrystalline Gallium Oxide in a Vitroceramic Composite: a Synchrotron X-Ray Diffraction Study, Phys. Rev. B, submitted (2008)
- K. E. Lipinska-Kalita, P. E. Kalita, O. A. Hemmers, T. Hartmann: Equation of State of Gallium Oxide to 70 GPa: Comparison of Quasihydrostatic and Nonhydrostatic Compression, Phys. Rev. B 77, 094123 (2008)
- K. E. Lipinska-Kalita, P. E. Kalita, C. Gobin, O. A. Hemmers, T. Hartmann, and G. Mariotto, Stability and equation of state of a nanocrystalline Ga-Ge mullite in a vitroceramic composite: A synchrotron x-ray diffraction study, Phys. Rev. B 77, 134107 (2008)
- K. E. Lipinska-Kalita, O. A. Hemmers, P. E. Kalita, G. Mariotto, S. Gramsch, R. J. Hemley, T. Hartmann: High-Pressure Structural Integrity and Structural Transformations of Glass-Derived Nanocomposites: a Review, J. Phys. Chem. Solids, 34, 8762 (2008)
- P. E. Kalita, A. L. Cornelius, H. P. Liermann, W. Yang, SRMS 5 - Rapid Communication, 221 (2006)
- K. E. Lipinska-Kalita, P. E. Kalita, D. M. Krol, R. J. Hemley, C. L. Gobin and Y. Ohki: Spectroscopic Properties of Cr^{3+} Ions in Nanocrystalline Glass-Ceramic Composites J. Non-Cryst. Solids 352, 524 (2006)

- K. E. Lipinska-Kalita, M. Pravica, G. Mariotto, P. E. Kalita and Y. Ohki: Core/Shell ZrTiO₄/ LiAlSi₂O₆ Nanocrystals: a Synchrotron X-Ray Diffraction Study of High-Pressure Compression, *J. Phys. Chem. Solids*, 67, 2072 (2006)
- K. E. Lipinska-Kalita, D. M. Krol, R. J. Hemley, P. E. Kalita and Y. Ohki: Temperature Effects on Luminescence Properties of Cr³⁺ Ions in Heterophased Oxide Glass Based Nanostructured Media, *J. Applied Physics* 98, 543021 (2005)
- K. E. Lipinska-Kalita, G. Mariotto, P. E. Kalita and Y. Ohki: Effects of High Pressure on Stability of the Nanocrystalline LiAlSi₂O₆ Phase of a Glass-Ceramic Composite: a Synchrotron X-Ray Diffraction Study, *Physica B: Condensed Matter* 365, 155 (2005)
- K. E. Lipinska-Kalita, D. M. Krol, R. J. Hemley, G. Mariotto, P. E. Kalita and Y. Ohki: Synthesis and Characterization of Metal-Dielectric Composites with Copper Nanoparticles Embedded in a Glass Matrix: a Multi Technique Approach, *J. Applied Physics* 98, 543011 (2005)
- K. E. Lipinska-Kalita, S. A. Gramsch, P. E. Kalita and R. J. Hemley: In situ Raman Scattering Studies of High-Pressure Stability and Transformations in the Matrix of a Nanostructured Glass-Ceramic Composite, *J. Raman Spectroscopy* 36, 938 (2005)

Thesis Title: Titanium Hydride up to 90 GPa: Synchrotron X-Ray Diffraction Studies

Thesis Committee:

Chairperson, Prof. A. Cornelius, Ph. D.
 Committee Member, Prof. M. Nicol, Ph. D.
 Committee Member, Prof. L. Zane, Ph. D.
 Graduate Faculty Representative, Prof. D. Lindle, Ph. D.